

# Deep Learning Based Object Tracking in Walking Droplet and Granular Intruder Experiments

Erdi Kara,<sup>\*†</sup> George Zhang,<sup>‡</sup> Joseph J. Williams,<sup>†</sup> Gonzalo Fernandez-Quinto,<sup>§</sup> Leviticus J. Rhoden,<sup>¶</sup> Maximilian Kim,<sup>||</sup> J. Nathan Kutz,<sup>†</sup> Aminur Rahman<sup>†</sup>

## Abstract

We present a deep-learning based tracking objects of interest in walking droplet and granular intruder experiments. In a typical walking droplet experiment, a liquid droplet, known as *walker*, propels itself laterally on the free surface of a vibrating bath of the same liquid. This motion is the result of the interaction between the droplets and the surface waves generated by the droplet itself after each successive bounce. A walker can exhibit a highly irregular trajectory over the course of its motion, including rapid acceleration and complex interactions with the other walkers present in the same bath. In analogy with the hydrodynamic experiments, the granular matter experiments consist of a vibrating bath of very small solid particles and a larger solid *intruder*. Like the fluid droplets, the intruder interacts with and travels the domain due to the waves of the bath but tends to move much slower and much less smoothly than the droplets. When multiple intruders are introduced, they also exhibit complex interactions with each other. We leverage the state-of-art object detection model YOLO and the Hungarian Algorithm to accurately extract the trajectory of a walker or intruder in real-time. Our proposed methodology is capable of tracking individual walker(s) or intruder(s) in digital images acquired from a broad spectrum of experimental settings and does not suffer from any identity-switch issues. Thus, the deep learning approach developed in this work could be used to automatize the efficient, fast and accurate extraction of observables of interests in walking droplet and granular flow experiments. Such extraction capabilities are critically enabling for downstream tasks such as building data-driven dynamical models for the coarse-grained dynamics and interactions of the objects of interest.

## 1 Introduction

Since the seminal works of Couder and co-workers [1, 2, 3], walking droplets have revealed a wide array of exotic behavior such as quantum-like phenomena [4, 5, 6, 7, 8], diffusive behavior [9, 10, 11], orbital dynamics [1, 12, 13, 14, 15, 16, 17], and nonlinear dynamics and chaos [18, 19, 20, 21, 22, 23]. Droplet tracking has been the crucial first step in characterizing the dynamical properties associated with these observations. The least technical way to track droplets is to manually identify the droplet at each timestep and record its location. However, this requires a prohibitive amount of human input. The primary bottleneck in automating this process is in droplet identification, after which recording the coordinates of the droplets is trivial.

<sup>\*</sup>Corresponding Author, [erdikara@spelman.edu](mailto:erdikara@spelman.edu)

<sup>†</sup>Department of Mathematics, Spelman College

<sup>‡</sup>Department of Applied Mathematics, University of Washington

<sup>§</sup>Department of Physics, University of Washington

<sup>¶</sup>Department of Mechanical Engineering, University of Washington

<sup>||</sup>Department of Civil and Environmental Engineering, University of Washington

Similar to vibrating fluid baths, pattern-forming phenomena in vibrated baths of granular matter received serious attention by Melo et al. [24] and Metcalf et al. [25], who both elucidated transitions between square-forming and stripe-forming parameter regimes. More complex behaviors can form, and the behavior of vibrated granular materials varies richly with the bed depth  $F$ , the dimensionless shaking parameter  $\Gamma = \frac{a\omega^2}{g}$ , the particle diameter  $d$ , and other particle properties such as the coefficients of friction and restitution [26].

The experiments with granular matter parallel those with hydrodynamic droplets: a much larger particle, known as the *intruder*, is included in the vibrating media, and for certain ranges of  $F$  and  $\Gamma$ , the intruder will travel the experimental domain, its movement both propelled and mediated by the sea of vibrating particles surrounding it. The terminology of an *intruder* in the granular system stems from the idea of a much larger particle intruding upon a collection of otherwise identical particles. [27], [28]. Generally, the much larger particle is (generally) carried to the surface by convective forces within the granular matter generated by the vibrations [29].

With an effective tracking algorithm, accurate long-time statistics of droplet and intruders can be extracted. These statistics are often used to compare the dynamics with that of analogous quantum systems. Sub-optimal tracking algorithms can potentially lead to incorrect statistical assessments and negatively affect the reproducability of experiments. Moreover, the lack of reproducibility and erroneous statistics can produce misinformed dynamical models of the underlying physical processes.

Deep neural networks have become the state-of-the-art method for image recognition applications. Yet there have been few studies leveraging deep learning based object detection and tracking methods for applications related to droplet dynamics in micro-fluids and cellular imaging. Some applications of deep learning such as droplet detection, sorting and classification are discussed in [30]. In [31, 32, 33], YOLO [34] combined with the object tracking algorithm Deep SORT [35] is used to track droplet motion in a class of microfluidic experiments and soft granular flows based on synthetic images generated via Lattice-Boltzmann simulations. In [36], Faster R-CNN[37] and YOLO are compared for droplet detection in several microfluidic experiments. However, to the best of our knowledge, there has been no deep-learning based investigation regarding extraction of walking droplets and granular intruders from real experiments.

Unlike other droplet systems, walking droplets prove to be quite difficult to track due to their odd, morphing geometries and highly nonlinear motion, in addition to being microscopic and lacking in texture and color. These difficulties are exacerbated by sub-optimal experimental setups such as poor lighting and/or low resolution video capturing. Thus it is clear that there is a need for more accurate tracking algorithms. This becomes even more essential as precise long-time statistics are imperative to distinguish quantum-like behavior from probabilistic noise.

There are several key differences between the behaviors and tracking of the walking droplets and the granular intruders. First, the larger size of the intruder compared to the hydrodynamic droplet means that we are less vulnerable to false positives. Second, while multiple droplets may collide and merge into a single droplet, the intruders will never merge, but instead collide and bounce apart. Indeed such collision events pose their own challenge for particle-tracking algorithms due to the large velocity and acceleration of the intruders after the collision. However, intruders never merging is convenient for running an experiment for very long periods; in turn, this is necessary as the slow and erratic motion of the intruders means longer experimental time is required in order for the intruder to meaningfully explore the domain. Finally, to our knowledge, there has never been an application of intruder identification and tracking in any similar granular flow experiments involving surface waves.

The remainder of the manuscript is as follows: In Sec. 2, we outline the data acquisition stages regarding walking droplet and granular intruder experiments. In Sec. 3, we detail the preparation of object detection datasets described in Sec. 2 and discuss the model training and testing. Then, in Sec. 4, we present our detection and tracking results. Finally, in Sec. 5 we conclude our study with discussions and future directions.

## 2 Data Collection

### 2.1 Walking Droplets

While experimenting with previously available droplet videos and detection methods, we noticed that variations in some experimental variables, namely lighting and droplet resolution, led to inconsistent detection accuracy. Therefore, to determine the optimal experimental setup which yields the best performance, we gathered 10 videos of droplets while varying five experimental parameters (lighting, droplet resolution, corral color, forcing amplitude, number of droplets) unilaterally. The specific parameter values used for each video are listed in the table ??.

Table 1: Experimental parameters for walking droplet videos

Experiment	Lighting	Resolution	Color	Amplitude (g)	# of Droplets
Control	Medium (6)	High	Black	1.47	1
Lights Off	Off (0)	High	Black	1.47	1
Lights Low	Low (1)	High	Black	1.47	1
Lights High	High (11)	High	Black	1.47	1
Two Droplets	Medium (6)	High	Black	1.47	2
Three Droplets	Medium (6)	High	Black	1.47	3
Res Low	Medium (6)	Low	Black	1.47	1
Res Mid	Medium (6)	Medium	Black	1.47	1
Faraday	Medium (6)	High	Black	1.53	1
Corral White	Medium (6)	High	White	1.47	1

All videos were captured with an iPad Pro mounted on a tripod at 720p (which are all 30fps except for Corral White which was 60fps). To reduce algorithmic workload and minimize distractions, the videos were cropped to only contain the corral region.

Experimental variables not listed were kept controlled to the best of our abilities. We first 3D printed identically-shaped black and white circular corrals using PLA. Then, we filled the corrals to the same height for each experiment with silicone oil. The forcing frequency was also kept at 60HZ for all experiments.

Different levels of lighting were achieved with a tabletop LED photography light as the only light source within the room. The LED light has 11 different illumination levels, of which we captured footage at level 0 (Lights Off), level 1 (Lights Low), level 6 (Lights Mid), and level 11 (Lights High). Varying droplet resolution is achieved by placing the iPad at different vertical distances from the corral. The closer the iPad is to the corral, the higher the droplet resolution.

Both the silicone oil fluid bath and the droplets on top appear and behave drastically different depending on whether the forcing is below or above the Faraday threshold. Thus, we kept the frequency of the forcing constant at 60HZ and varied the amplitude to stay just below the Faraday threshold (1.47g) and to exceed the threshold (1.53g).

### 2.2 Granular Materials

The granular matter experiments share some similarities to the walking droplets experiments, but differ in some key ways. First, the bath of smaller particles consists of chrome steel bearing balls of  $d = 1.6$  mm and a bed depth of  $F = 7.5$  mm. The bath is enclosed in a cylindrical container with  $D = 214$  mm. We use intruder particles of two different ceramics, silicon nitride ( $\text{Si}_3\text{N}_4$ ) and zirconium oxide ( $\text{ZrO}_2$ ), both less dense than chrome steel. The intruders are sized  $d = 9.5$  mm.

Key differences in the experiments are found in the hyper-parameters. Neither lighting nor resolution were hyper-parameters for the granular matter experiments, but intruder color was. The  $\text{Si}_3\text{N}_4$  ceramic is white and the  $\text{ZrO}_2$  ceramic intruders are black. Identity switching is more likely when intruders of the same color are interacting with each other. The color of the corral was not varied. Reference Table ?? for the experimental parameters of our granular systems.

Table 2: Experimental parameters for granular intruders videos

Experiment	Intruder Material	Intruder Color	Amplitude (g)	Frequency $f$	# of Intruders
3white	3x $\text{Si}_3\text{N}_4$	3x White	2.26	20	3
2white2black-long	2x $\text{Si}_3\text{N}_4$ , 2x $\text{ZrO}_2$	2x White, 2x Black	2.15	20	4
2white2black-short	2x $\text{Si}_3\text{N}_4$ , 2x $\text{ZrO}_2$	2x White, 2x Black	3.10	50	4

As with the walking droplets, the granular experiments were also filmed with an iPad Pro mounted on a tripod at 720p and 30fps and the videos were cropped. The frequency and amplitude of the vibrations were varied across the experiments to ensure sufficient wave patterns and intruder activity.

### 3 Deep Learning Based Object Detection

As a fundamental computer vision problem, object detection is the task of locating objects and categorizing them into predefined classes in images or video frames. Autonomous driving, video surveillance systems, and real-time scene understanding are just a few applications of object detection.

Conventionally, object detection has been achieved without neural networks and deep learning. Image processing techniques such as the Hough transform and edge detection extract information from images by applying pixel-level operations or filters [38, 39, 40, 41, 42, 43, 44]. Background subtraction excels in extracting moving foreground objects in front of static backgrounds [45, 46, 47, 48, 49, 50, 51, 52]. Machine learning approaches such as the Viola-Jones algorithm train to detect objects given labelled data [53]. Successful implementations of image processing [54, 55, 56, 57, 58, 59], background subtraction [60, 61], and more recently machine learning techniques [62] have been readily reported in agricultural and biological contexts and, to our interest, on various forms of droplets. Readers can consult [63, 64, 65] for a more comprehensive review of commonly applied computer vision methods. While these techniques are not the main focus of our paper, we acknowledge their ability and viability. Thus, see Sec-4.2 and Appendix A for the detection results of these methods on walking droplets. In addition, we note that the background subtraction problem typically assumes a static background. However, the droplet and intruder system both have objects of interest whose background is also dynamics. For instance, the granular material is dynamic as the intruder evolves over its trajectory. This makes the detection problem more challenging.

As the complexity and amount of experimental data increases, conventional feature extraction processes have difficulty providing effective detection and tracking results. In the last 10 years, deep neural networks achieved breakthrough results particularly in image recognition domain. In terms of performance, many of these conventional methods were surpassed by neural networks in almost all image recognition applications including object detection. Since the full review of deep learning based object detection literature is beyond the scope of this paper, readers may consult to [66, 67] for an extensive review of current state of this field.

In this work, we use the YOLO architecture proposed by Redmon et.al in [68]. Since then, it has been extensively adopted in computer vision research due to its fast and accurate object detection capabilities in real time. In the subsequent years, the model was gradually improved resulting in several versions [69, 70, 71] and achieved state-of-art results on the most commonly used object detection datasets such

as Pascal VOC and COCO [72, 73].

YOLO frames the object detection problem as a regression task. As a supervised machine learning framework, YOLO must be optimized on a training dataset. In this case, the training data is composed of images and bounding box coordinates of the object classes present in each image. Each input image is divided into  $S \times S$  regular rectangular grids. For each grid, the model predicts  $B$  bounding boxes represented by the box center coordinates (relative to the cell) and the width and height (relative to the entire image). A confidence score  $CS$  and conditional class probability  $Pr(C_i)$  are also part of the model output. Confidence score  $CS$  is calculated as

$$CS = Pr(\text{Object}) \cdot IOU \quad (1)$$

where  $Pr(\text{Object})$  indicates the probability that the grid contains an object belonging to any of the pre-defined classes. While values close to 0 indicate the absence of an object in that particular grid, values close to 1 point to the presence of an object. The *intersection-over-union* (IOU) is one of key metrics in object detection problems that measures the degree of overlap (0 being no overlap, 1 being complete overlap) between the bounding box prediction and the ground truth bounding box. In model training or testing stages, one can set certain IOU threshold values to decrease the number of false positive identifications. The conditional class probability is computed as

$$Pr(C_i) = Pr(C_i|\text{Object}), \text{ for } i = 1, 2, \dots, N \quad (2)$$

where  $N$  is the number of classes.  $Pr(C_i)$  is a direct measure of the probability of the object belonging to the class  $C_i$ . The model outputs one set of probabilities per grid. Note that if the grid does not contain any object,  $Pr(C_i)$  must be zero. As a result, for a single image, YOLO produces a tensor of size  $S \times S \times (5B + N)$ , which is the prediction of the output layer of the YOLO network. Finally, this output is passed through a Non-Maximal suppression algorithm, eliminating the bounding boxes with low confidence scores. Once the output is obtained, YOLO computes the error via a *multi-component* loss function which is composed of localization error for bounding box predictions and the classification error for conditional class probabilities [68]. The confidence score associated with each box is readily available during training phase. In testing time, it is a predicted quantity calculated by the network. For droplets and intruders, the number of classes  $N = 1$ . Thus, whenever the object is predicted present in the image, the confidence score reduces to  $IOU$ .

We lastly discuss the concept of *mean average precision (mAP)* which is one of the most common metrics used in object detection problems. This is a single number between 0 and 1 measuring the accuracy of the network across the dataset in consideration. To compute mAP, we first calculate precision (P) and recall (R) using the following formula

$$P = \frac{TP}{TP + FP} \quad , \quad R = \frac{TP}{TP + FN} \quad (3)$$

In (3), TP represents the number of true positives, i.e, droplet is present and detected while TN indicates the number of true negatives, i.e, droplet is not present and not detected. FN is the number of false negatives, i.e, the droplet is present but not detected while FP is the number of false positives, i.e. the droplet is not present but detected. Notice that to classify a detection as TP or FP, a threshold value must be imposed. In the object detection problem, it is very common to choose an IOU to set this threshold. In this work, we report the mAP metric with the threshold value  $IOU = 0.5$ . In other words, whenever  $IOU \geq 0.5$ , we classify this detection as a true positive. Once we set the threshold value, we obtain precision and recall values and consider precision as a function of recall. Formally, the average precision (AP) is defined as

$$AP = \int_0^1 P(r)dr \quad (4)$$

where mAP is calculated among all predefined object classes in the dataset. This metric is known as *mAP@.5* when the threshold is set to  $IOU = 0.5$ . Another common metric is *mAP@[.5:.95]*. In this case, IOU threshold is varied from 0.5 to 0.95 and mAPs registered for each separate threshold are averaged out to obtain a single *mAP@[.5:.95]* score.

### 3.1 Data Preparation

The following tables detail the properties of each video regarding the walking droplet experiments introduced in Sec-2.1 as well as the number of training, validation and testing images utilized to train and test the YOLO architecture described above.

Table 3: Summary of each walking droplet experiment

Experiment	Duration(mins)	Frame Count	TrainImg	ValidImg	TestImg
Control	4.31	7494	120	34	17
Lights off	4.53	7884	126	36	18
Lights low	4.58	7962	127	36	18
Lights high	4.27	7426	124	36	17
Two droplets	4.62	8032	129	36	18
Three droplets	5.19	9034	127	36	18
Res mid	5.63	9798	123	35	17
Res low	4.49	7805	125	36	17
Faraday	4.67	8118	130	37	18
Corral White	2.08	7692	126	36	17

Our general approach for walking droplet experiments is to employ around 180 frames that are sampled with uniform time intervals from the corresponding video source. Out of these frames, we then reserve 70% for training, 20% for validation, and 10% for testing. Notice that we consider only around 2% of the frames relative to the total number of frames present in the video sources. Since data preparation takes up the largest chunk of time in model training, it is essential to keep the training data as small as possible without compromising the model accuracy. In particular, the droplets in our dataset are approximately squares 6-10 pixels wide which renders manual bounding box annotation particularly challenging. But using more training images does generally result in better performing models. We will detail our choice regarding the number of images to train our model in Sec-4.1. Therein, we train separate models for Control and Three Droplets experiments by increasing the number of training images. It appears that the model performance starts to saturate around 80-100 images. Based on this observation, we opted to consider a slightly conservative estimate and created 120 training images from each experiment.

Regarding granular intruder experiments, the datasets used for model training are summarized in Table-4. Notice that we employ considerably less images compared to droplet experiments. As it will be detailed below, large and distinct shapes of intruders relative to their surrounding medium significantly helps the YOLO model to learn from a small number of training samples. Due to the same reason, we do not create a separate annotations for the 2white2black-short experiment since the intruders in both experiments are qualitatively similar.

Table 4: Summary of each granular material experiment

Experiment	Duration(mins)	FrameCount	TrainImg	ValidImg	TestImg
3white	7.04	7884	31	8	4
2white2black-long	20.22	36259	31	8	4
2white2black-short	10.31	17893	-	-	-

As noted above, object detection datasets are usually composed of images and the coordinates of the bounding boxes associated with each object of interest in the corresponding image or frame. To create our dataset, we used the online annotation tool *LabelImg* [74].

### 3.2 Model Training

In this work, we adopted the Pytorch [75] implementation of the YOLO architecture maintained by Ultralytics in [76]. In particular, we selected the YOLOv5 architecture which is one of the fastest and lightweight implementations of YOLO. One can train a separate model for each of the experiments above or a single model by combining the individual datasets. For simplicity, we use the single model option. However, we experimented with the former as well and observed similar results in both cases.

While the combined walking droplet dataset is composed of 1257 training, 358 validation and 175 testing images with their annotations, the granular flow dataset has 62 training, 16 validation and 8 testing images. We trained the models with pretrained COCO weights and used the default set of hyperparameter configuration provided by the same repository [76]. The model regarding droplet data was trained for 63 minutes with 285 epochs. The granular experiment training was carried out for 4.6 minutes with 300 epochs. On the validation set, the droplet model's mAP@.5 and mAP@[.5:.95] scores were recorded as 0.995 and 0.532, respectively. The granular flow model's mAP@.5 and mAP@[.5:.95] scores were observed to be 0.995 and 0.715, respectively. In each training session, the model with the best mAP@.5 is saved and its performance is verified on the test data which was not seen by the model. For the testing data, our droplet model achieved 0.982 mAP@.5 and 0.48 mAP@[.5:.95] while the granular flow model scored 0.995 mAP@.5 and 0.672 mAP@[.5:.95]. These results are summarized in Table-5.

Table 5: Training results

Experiment	Time	Epochs	Validation		Test	
			mAP@.5	mAP@[.5:.95]	mAP@.5	mAP@[.5:.95]
Walking Droplet	63	285	0.995	0.532	0.982	0.48
Granular Flow	4.6	300	0.995	0.715	0.995	0.672

Fig-1 demonstrates the evolution of mAP@.5 and mAP@[.5:.95] over the course of model training. In both cases, we can observe that the mAP@.5 values gradually increase and saturate around 1 which points to a perfect accuracy.

All training and testing stages were performed on a GE66 Raider 10SFS with a 2.60GHz Intel Core i7-10750H CPU and an NVIDIA GeForce RTX 2070 Super GPU.

## 4 Results

### 4.1 Walker and Intruder Detection

Once we have a trained model accurately detecting droplets, we can process the walking droplet and granular flow videos on a frame-by-frame basis and detect the walker or intruder locations in each frame.

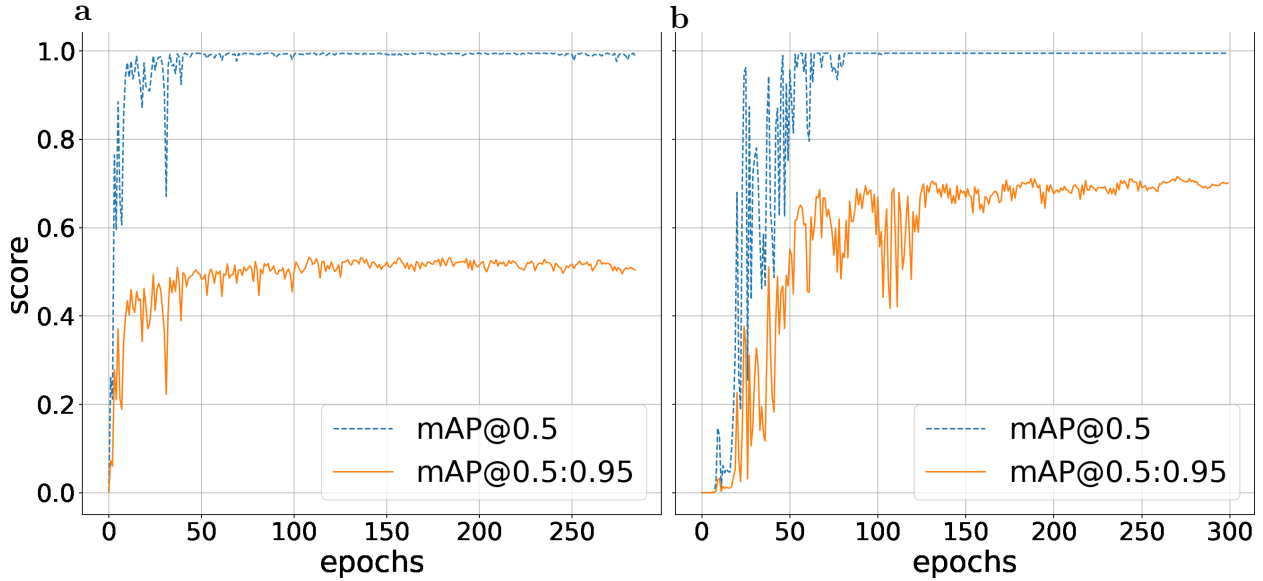


Figure 1: Training performance of the droplet model (a) and granular flow model (b). The yellow solid curve (bottom) represents the performance of mAP@0.5:0.95 and the blue dashed curve (top) represents the performance of mAP@0.5.

We perform this operation in real-time. For each frame in the corresponding video source, we accept a detection is valid only if the detected number of droplets or intruders is equal to the number of droplet(s) or intruder(s) in the related experiment. Moreover, we strictly impose that the confidence score associated with each droplet or intruder detection must be above a certain threshold value. In this work, we set this threshold to 0.45. For example, if we consider three-droplet experiment, we accept a detection valid only if it detects exactly three droplets with a confidence score above 0.45. Note that since the size of the droplet is small compared to the actual frame and the droplet itself is composed of the same fluid as the medium, one may encounter false-positives either on the medium or even on the experiment tray. Although this effect appears to be less pronounced in granular experiments, we would like to maintain relatively high confidence for each intruder as well. As detailed in the next section, one of the primary goals of this paper is to extract the individual droplet or intruder trajectories. Such a criteria helps us avoid false-positive identifications which essentially renders the extracted trajectory unreliable. Using this approach, we count how many frames fulfill this criteria and define *frame detection rate* (FDR) as the ratio of frames passing this criteria to the total number of frames. The results in 6 and 7 demonstrate a near perfect performance of the YOLOv5 model. Due to the accurate detection capabilities of the model combined with the aforementioned criteria, we do not observe any false-positive identifications in any of the experiments. Readers are highly encouraged to watch the real-time detection videos of each experiment provided in the supplementary material.

Table 6: Frame detection rates for walking droplet experiments

Experiment	Total Detections	Total Frames	Frame Detection Rate
Control	7491	7494	0.9996
Lights Off	7859	7884	0.9968
Lights Low	7956	7962	0.9992
Lights High	7391	7426	0.9953
Two Droplets	7824	8032	0.9741
Three Droplets	8657	9034	0.9583
Res Mid	9768	9798	0.9969
Res Low	7752	7805	0.9932
Faraday	7998	8118	0.9852
Corral White	7542	7692	0.9805

Table 7: Frame detection rates for granular flow experiments

Experiment	Total Detections	Total Frames	FDR
3white	12530	12720	0.98
2white2black-short	17893	18918	0.95
2white2black-long	36259	36663	0.98

In terms of detection, the model achieves near perfect detection rate in a wide spectrum of experimental settings. We should note that one can attempt to create an extremely challenging experimental setting to drastically lower the model performance or potentially break the process all together to test the limits of the proposed methodology. In the context of our study, we argue that such an attempt is not the focus of the experiments in consideration. To extract proper trajectories of walking droplets and granular materials, experiments should be conducted in favorable conditions such as maintaining even lighting and utilizing a stable camera setup capable of high resolution videos. However, we acknowledge the possibility for external noise in the process of gathering video samples. Thus, we demonstrate that the proposed methodology is well suited for even the most extreme circumstances encountered such as low/bright lighting, variability in resolution and frame rate, nonlinear motion of the objects and so on.

The near perfect detection presented in Table-6 and 7 will constitute the most important component of the trajectory extraction task which is the overarching goal of this paper. To emphasize the importance of accurate detection, let us consider the Three Droplets experiment where the model is capable of detecting 8657 out of 9034 frames. The corresponding experiment video is captured approximately 30 frame-per-second (fps) with a length of 5.19 minutes. This means the model is missing only 12.5 seconds out of 5.19 minutes. We carefully note that those undetected frames are scattered across different times in the video. Thus, its effect on trajectory extraction is essentially negligible. Similarly, the model is missing only 24 seconds out of 22.22 minutes in the 2white2black-long granular experiment. Maintaining a near perfect frame detection rate is particularly important for experiments including multiple walkers or intruders. This point will be detailed in Sec-4.3.

Some detection samples with bounding boxes and their associated confidence scores are displayed in Fig-2. Samples in the top rows are from the test dataset of the Three Droplets and Two Droplets experiments while the bottom ones are taken from the Lights Off and Faraday experiments. In each instance, the droplets are accurately detected with high confidence.

Notice the usage of black corrals in all of the experiments except one. We carried out one experiment with a white corral holding a walker in an attempt to test the performance of YOLOv5 in a more demanding setting. As opposed to the previous experiments which are all 30 fps, we also captured this

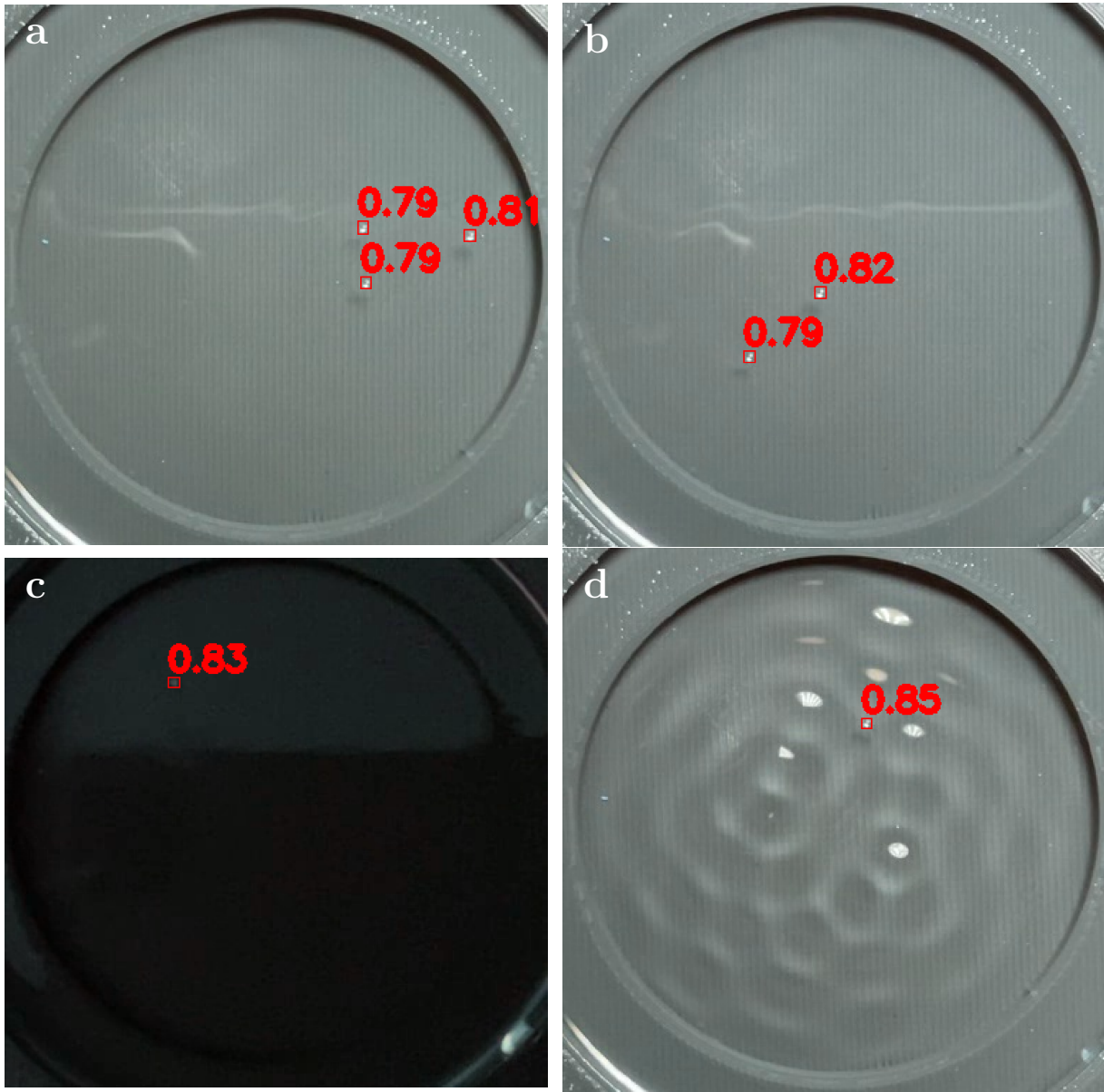


Figure 2: Walking droplets detection samples from our implementation of YOLOv5. The red solid square indicates YOLOv5 finding the walker, and the decimal values next to the square indicate the confidence score in the range of 0 to 1. **(a)** and **(b)** Videos selected from the test dataset of the “Three Droplets and Two Droplets” experiments. **(c)** and **(d)** Videos selected from the “Lights Off and Faraday” experiments.

experiment at 60 fps. The outlined procedure was still capable of capturing 98% of the frames despite the walker blending into the background. As seen in Fig-3, YOLOv5 has no difficulties in detecting the walker in a white corral, which may be a challenging task even for human vision.

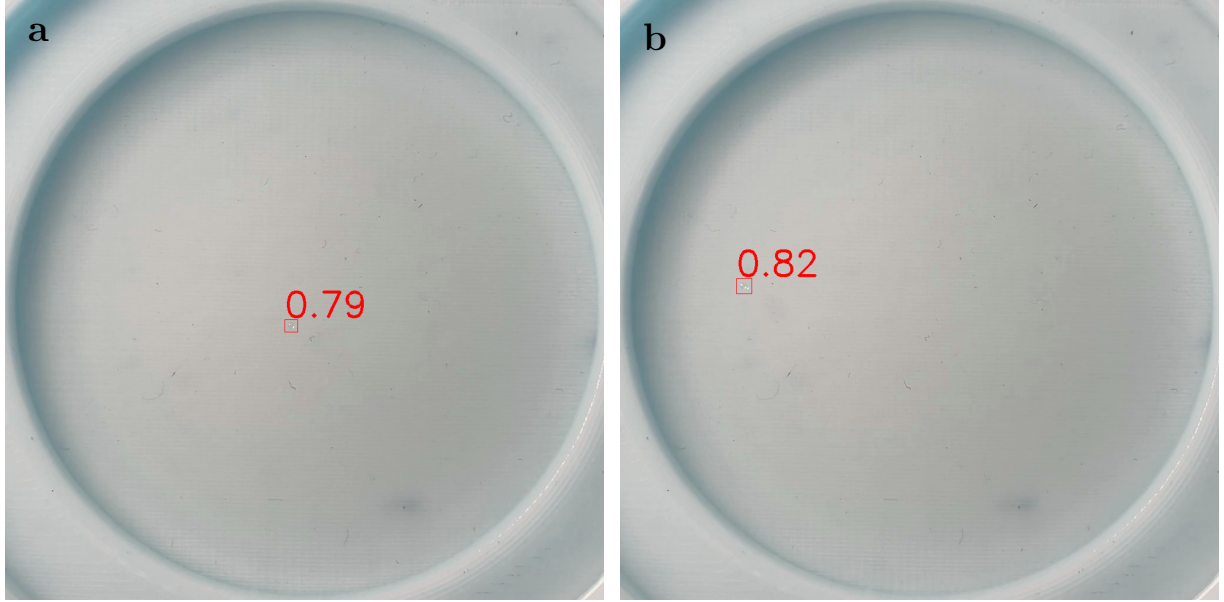


Figure 3: The walker captured by YOLOv5 in the “White Corral” video in two separate frames. The red solid square indicates YOLOv5 finding the walker, and the decimal values next to the square indicate the confidence score in the range of 0 to 1.

Similarly, the model can detect the intruders in the granular material experiments with high confidence. We display some samples in Fig-4.

Data preparation is a major bottleneck in supervised machine learning. In particular, manual annotation of training images in object detection problems is a labor-intensive process. For our experimental settings, Table-6 and Table-7 indicate that we can achieve near-perfect detection accuracy with around 120 training images for droplet experiments and 30 training images for granular flow experiments. Note that these are just a tiny fraction of the total number of frames in the corresponding video sources. However, one can determine the approximate number of training images that will likely yield a high detection rate prior to actual model training. Such an investigation would be particularly useful in cutting annotation time if qualitatively similar experiments are to be carried out multiple times. One way of investigating the optimal number of images would be to gradually increase the number of training images by respecting 70%:20% ratio between them and keeping the same number of testing images. We can then plot mean average precision as the function of the number of training images and analyze if the function displays an asymptotic behavior around a mAP score of 1. For example, let us consider the Control experiment for which we initially created 120 training, 34 validation and 17 testing images. We can fix the validation and testing data and train the model by gradually increasing the number of training images from 5 images to 120 images and each time keeping appropriate number of validation images. For each training cycle, we use the very same 17 testing images. Since this is just a preliminary investigation, we set the number of epochs to 50 for each training cycle. Figure-5 displays the results of this investigation for the Control (left) and Three Droplets (right) experiments. In both cases, we can observe the mAP@0.5 values fluctuating around 1 when the number of training images exceeds 60. Based on similar investigations of other experiments, we set the number of training images to a conservative estimate of 120.

Recall that we trained a single model for the dataset that is composed of around 120 training images

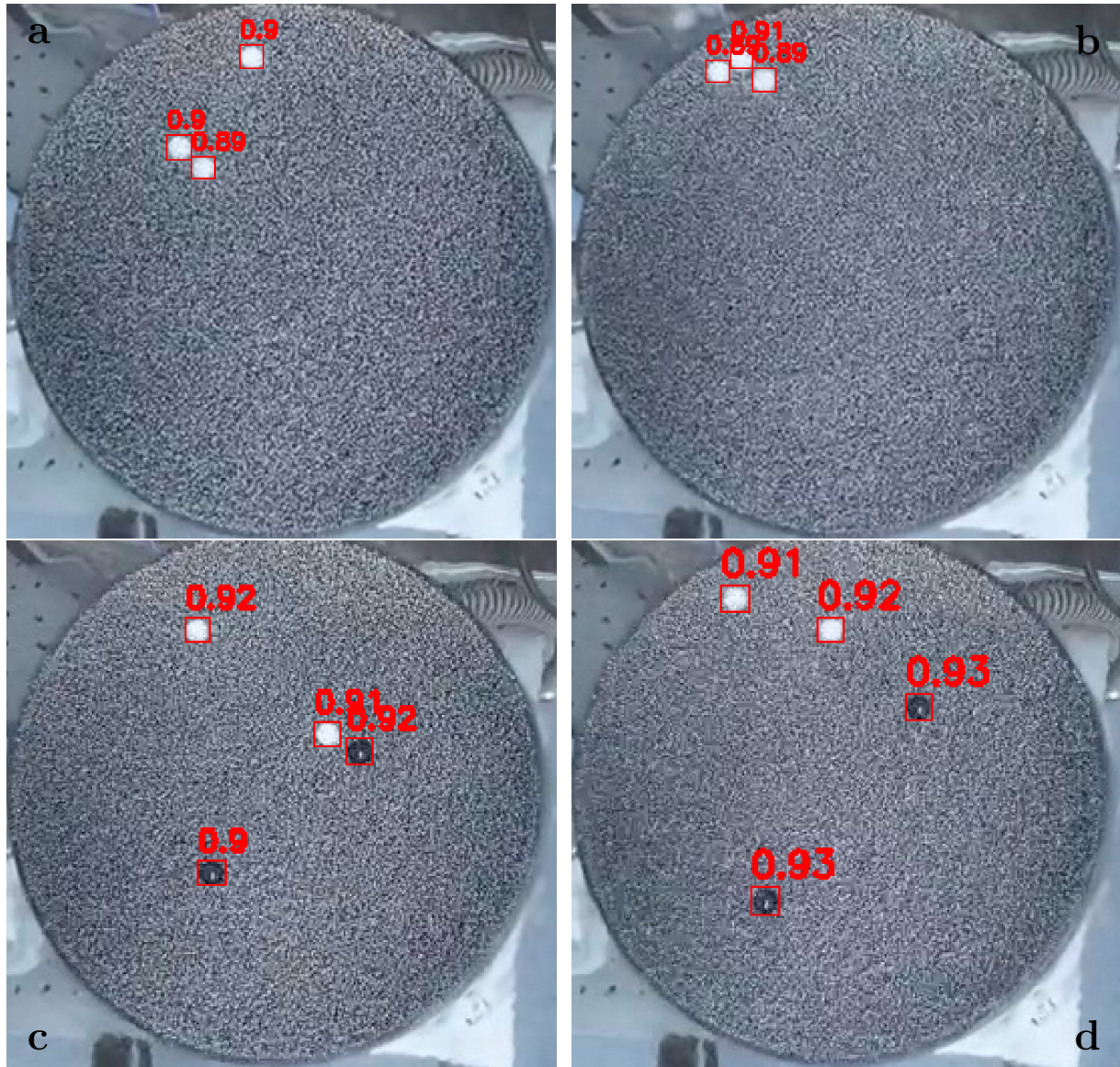


Figure 4: Granular material detection samples by our YOLOv5 model from experiments with three white intruders (a, b) and two white and two black intruders (c, d). The red solid square indicates the walker, and the decimal values next to the square indicate the confidence score in the range of 0 to 1.

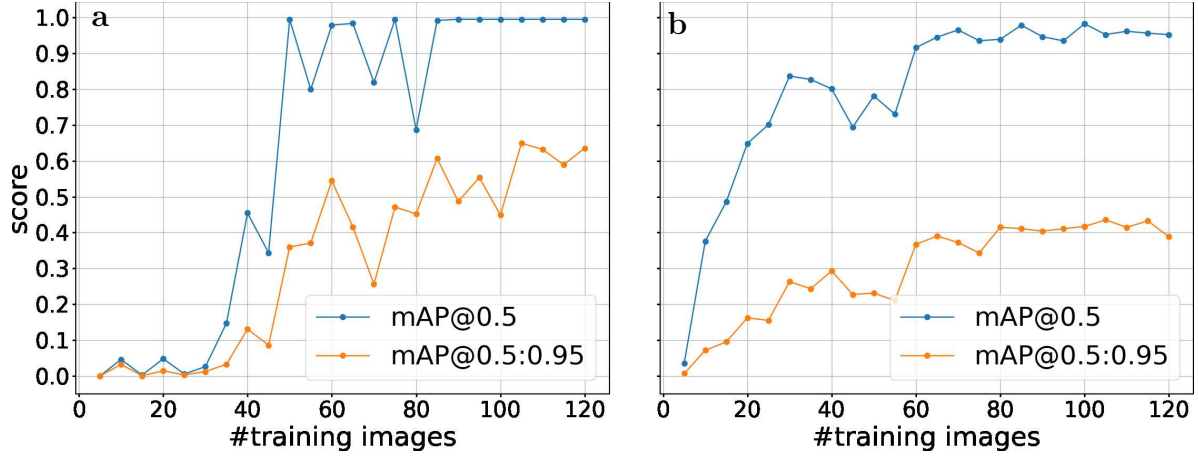


Figure 5: Model performance of the Control **(a)** and three droplet **(b)** experiments. The yellow solid curve (bottom) represents the performance of  $\text{mAP}@0.5:0.95$  and the blue dashed curve (top) represents the performance of  $\text{mAP}@0.5$ .

taken from each experiment. However, one can use fewer number of images if the goal is to train a separate model for each experiment. For example, the right panel in Fig-5 indicates that one can employ around 50 training images for Three Droplets experiment without compromising from the model performance. This is indeed correct. With 50 training, 14 validation and 7 testing images, it takes around 3.5 minutes to train the model and the model still achieves 99.28% detection rate. We should also note that the very same model trained for Three Droplets equally performs for Control experiment but not for Lights Off or Corral White. This difference can be explained by the degree of variability between the experiments. Therefore, it may be more practical to train a single model in case of multiple experiments rather than dealing with training multiple models.

## 4.2 Conventional Detection Methods

Although novel deep learning object detection methods such as YOLOv5 might be the most robust, conventional methods may still have their uses. In exchange for cutting-edge performance, these techniques offer simplicity, interpretability, and speed. We consider three categories of computer vision techniques, with each having its own trade-offs: image processing, background subtraction, and the Viola-Jones algorithm.

Using the Hough transform algorithm for circle detection to locate droplets forms the basis of our image processing procedures. By performing Canny edge detection prior to the Hough transform, we can eliminate much of the noise within the image and achieve relatively high recall and precision under most experimental conditions. Consistency may be an issue as the Canny edge detection method produces false negatives as the resolution of the droplets varies. Image processing techniques offer high interpretability compared to black box machine learning algorithms and do not require training images. Some parameters need to be tuned but image processing techniques are typically fast to run once set up. Out of the three background subtraction variations we tested, KNN performed well under most circumstances. While not perfect, it demonstrated a higher consistency compared to image processing techniques and remains easy to set up and fast to run without needing labeled training images. Note that the experimental setup must be stable and undisturbed for background subtraction to function properly. The Viola-Jones machine learning algorithm requires training images but could not accurately locate droplets, the reason likely

being the small size and minimal texture of the droplets.

In general, none of the conventional methods could match YOLOv5 in performance nor achieve any form of accuracy when Faraday waves formed and when the corral was white. While the Canny edge detection and KNN background subtraction methods might be applicable in some controlled environmental settings, YOLOv5 is preferred for rigorous studies. For the details of our findings see Appendix A.

### 4.3 Trajectory Extraction by Object Tracking

The ultimate goal of our efforts in this study is to accurately describe the dynamics in walking droplet and granular intruder experiments with minimal human input and to automate this process. In particular, we would like to obtain the trajectories of the individual objects of interests in the experiments described above. In terms of computer vision tasks, this falls under the category of object tracking.

Object tracking refers to assigning unique identities to objects in an image and tracking them in the subsequent frames. In computer vision, this task is defined as multiple object tracking (MOT) or single object tracking (SOT) depending on the task. The essential step in object tracking is first detecting the objects. Thus, all the challenges present in object detection problems inherently exist for object tracking as well. Occlusion, nonlinear motion, appearance or disappearance of objects between the frames and similar visual features of the objects are just a few difficulties that make object tracking a challenging task. Failure of a tracker can manifest itself in different forms. Trackers may lose an already tracked object, confuse the initial object identities with other class identities in the subsequent frames resulting in *identity switches* (*ID switch*) or fail to track the objects all together. If the ultimate goal of the study is to accurately identify the trajectory of an object, the tracker must be free of these defects to a great extent. Since the development of a new MOT framework is not the focus of this work, the reader is encouraged to consult excellent review articles which give a comprehensive review of MOT methods and approaches [77, 78, 79]. Among the existing methods, the most common approach is tracking-by-detection which works in two stages. In the first stage, the object of interests are located in the scene. In the second stage, these object are associated with already tracked ones by a tracking model. Most of the MOT algorithms are equipped with some or all of the following features; (1) detection, (2) feature extraction (e.g with the help of neural networks) or motion prediction (e.g Kalman Filter), (3) affinity and (4) association. [79]

We demonstrated in the previous section the high performance of our YOLOv5 model in (1) for various forms of experiments in consideration. As it is the case in many machine learning tasks, it is essential to integrate domain specific knowledge into the problems we tackle. In the context of our experimental settings, the number of walker or intruders essentially dictate the number of objects detected per frame since disappearance of an existing walker or intruders or appearance of new ones are not allowed. For example, we terminate the experiment if any coalescence between walkers occur. Therefore, false-positive identifications can be handled to a great extend by only considering frames where the detection count matches the actual walker or intruder count and imposing a high confidence score on detections. However, as detailed below, high and accurate detection rates may not guarantee accurate tracking even if one employs a state-of-the-art object tracking framework.

Given the accurate detection performance of YOLOv5, the task is to build a tracker which is capable of tracking each individual walker or intruder in our experiments. Several issues remain post-detection that render droplet or intruder tracking a very challenging task. Droplets in our experiments are only 7-10 pixels across, lack rich visual context and exhibit highly nonlinear motion, especially when they collide. A similar challenge is also present in granular intrude experiments as the shape and visual properties of intruders are quite similar to each other. The extremely small size and almost identical appearance of the walkers or intruders combined with chaotic motion are fundamental obstacles that hinder the performance of the tools employed in (2). Even with deep neural networks, feature extraction cannot assist in tracking given nearly indistinguishable droplets. Motion detection fails and can even lead to identity switches when

the motion of walkers or intruders follow no perceivable pattern.

At this point, we can turn our attention to one of the state-of-the-art tracking libraries and implement some of them for our problem. However, we argue that one can employ a solely motion based tracking method to solve this problem. In this sense, we employ the Hungarian Algorithm which solves the linear assignment problem (sometimes called 2-assignment problem) in polynomial time [80]. Let  $\{c_i^{(f)}\}_{i=1}^n$  and  $\{\hat{c}_i^{(f+1)}\}_{i=1}^n$  be the center of the bounding boxes representing the location of  $n$  droplets detected in two adjacent frames  $f$  and  $f + 1$ . In literature,  $\{c_i^{(j)}\}_{i=1}^n$  and  $\{\hat{c}_i^{(j+1)}\}_{i=1}^n$  are sometimes called *tracks* and *detections*, respectively. We define the following cost matrix based Euclidean distance

$$C(i, j) = \|c_i - \hat{c}_j\| \text{ for } i, j = 1, 2, \dots, n \quad (5)$$

Hungarian algorithm aims to identify  $n$  unique indices from  $C$  in a way that there is one index in each row and in each column such that the total cost associated with these  $n$  indices is minimized. Once these unique indices are identified, they are added to the tracks and the process is repeated. In the actual implementation of the Hungarian Algorithm, we utilized the Scipy library [81]. The Hungarian Algorithm can be considered as one of the most simplistic approach for MOT problems. Due to its simplicity, it is regarded as a typical base model in object tracking benchmarks.

In spite of its simplicity, the Hungarian Algorithm is well suited to our problem setting. As noted above, walkers and intruders in our experiments have almost identical visual appearances. Therefore, the feature extraction stage used by many MOT methods may fail to differentiate those similar objects from one scene to the next. Moreover, motion predictor functionalities in MOT frameworks do not perform well if the object of interests exhibit highly nonlinear motion between consecutive frames. Therefore, we argue that the Hungarian Algorithm, which is not corrupted by potentially negative effects of feature extraction and motion prediction, is an ideal option to track the individual walkers and intruders. To investigate these arguments, we compared the Hungarian Algorithm with StrongSORT [82], which is one of the state-of-the-art object tracking frameworks. We found that while StrongSORT suffers from multiple ID switches, the Hungarian Algorithm is completely free of ID switches in our walking droplet experiments with multiple droplets and our granular flow experiments. StrongSORT's failures usually occur during close interactions of visually similar walkers or intruders within a short distance of each other. This point will be detailed in the Sec-4.4.

Note that one can replace the Euclidean norm with Intersection over Union (IOU) similarity in 5 and find the index set that maximizes the cost as well. However, IOU is not a useful measure of similarity because the similar size of the walkers and intruders with their almost identical appearances result in low variability in IOU scores. Figure-6 demonstrates IOU scores for each droplet detection in three subsequent frames of the Three Droplets experiment. Notice that IOU scores are actually the same up to the first significant digit. Thus, for our particular problem, a tracker whose (3) affinity and (4) association stages that solely rely on IOU is highly likely to suffer from multiple misidentification of walkers or intruders.

We first present the tracking results regarding the single and multiple droplet cases and extract important information to further analyze the characteristics of droplet motion. Our primary goal is to keep track of the coordinates of the bounding box centers for each individual droplet. In particular, we would like to perform this task in real-time. We present three snapshots from the Control and Lights Off experiments in Fig-7. Since there is only a single droplet in these experiments, an initial ID = 0 is assigned to the droplet and the same ID is tracked in the subsequent scenes. Since our approach is purely motion based, there is no ID switch in any of the single droplet experiments. We also note again that we are capable of tracking 99% of the 7482 frames in the Control experiment and 7869 frames in the Lights Off experiment by using only around 120 training frames for each experiment. For all the other experiments, the reader is highly encouraged to watch the real-time tracking videos provided in the supplementary material.

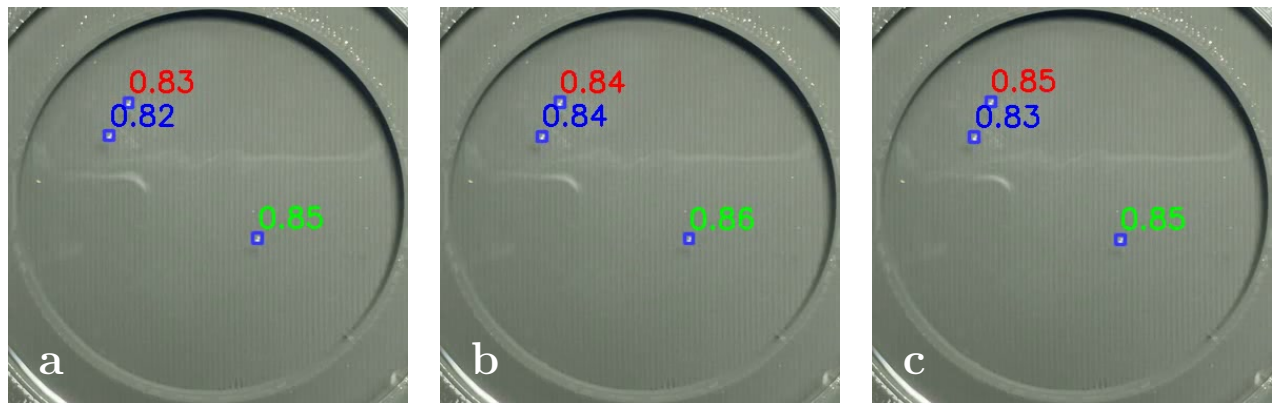


Figure 6: Low variability in the Intersection over Union metric in three subsequent frames for walking droplets. The blue solid square indicates YOLOv5 finding the walker, and the decimal values next to the square indicate the confidence score in the range of 0 to 1.

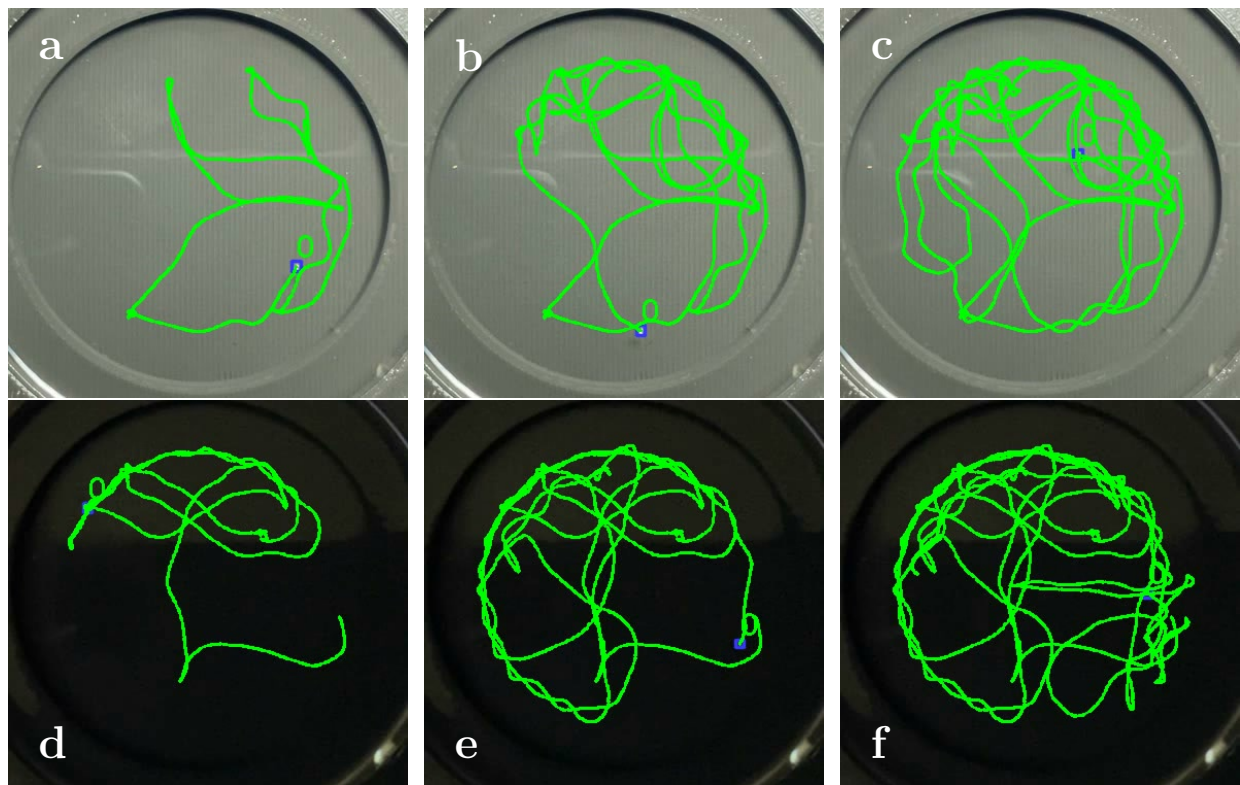


Figure 7: Real time tracking of walking droplets from the Control (a, b, c) and Lights Off (d, e, f) experiments at three different time snapshots.

Note that single droplet tracking is not challenging as long as the detection algorithm accurately identifies the location of the droplet. Once a single location is identified, association with the previous frame is straightforward since there is no another droplet present in the frame. However, multiple droplet experiments pose several characteristics which renders tracking very challenging. One particular challenge is the nonlinear nature of the droplet motion that may include rapid accelerations from one frame to the next. In particular, the moment when two or more walkers approach each other, they generally experience a push stemming from the superposition of pilot waves. This in return causes walkers to rapidly accelerate between two consecutive frames. To avoid ID switches, we heavily rely on the ability of YOLOv5 to resolve the motion, i.e. it keeps detecting the droplets with high confidence. Similar to single droplet experiments, we have not observed any ID switches in multiple droplet experiments. Fig-8 demonstrates several snapshots captured from the Two Droplets and Three Droplets experiments. For ease of visualization, we use a different color for each track representing the trajectory of individual droplets. As mentioned above, these results are essentially observed in real time with no external post-processing. In other words, we save and display the trajectories simultaneously until the end of the corresponding experiment. As expected, the trajectories appear to be chaotic rather than following a regular path.

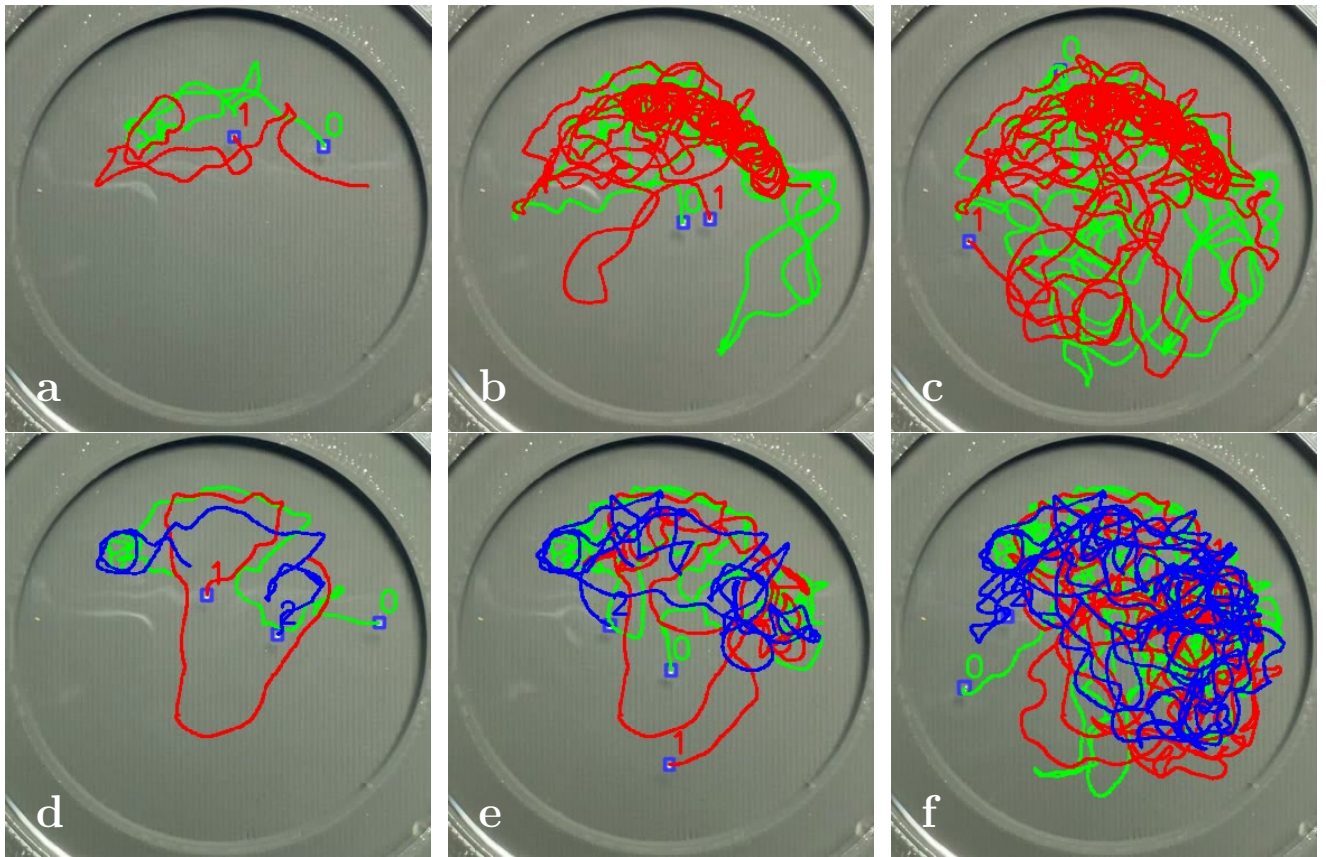


Figure 8: Real time tracking snapshots from the two (a, b, c) and three (d, e, f) droplet experiments. The snapshots were taken at  $t = 20\text{s}$  for (a),  $t = 147\text{s}$  for (b),  $t = 250\text{s}$  for (c),  $t = 10\text{s}$  for (d),  $t = 63\text{s}$  for (e), and  $t = 202\text{s}$  for (e). The different colors represent the different individual droplets.

Similarly, we can extract the trajectories of individual intruders in granular flow experiments. Figures in Fig-9 indicate that the intruders exhibit significantly less displacement than walking droplets.

Once the locations of the individual walkers or intruders are correctly identified, we can further analyse

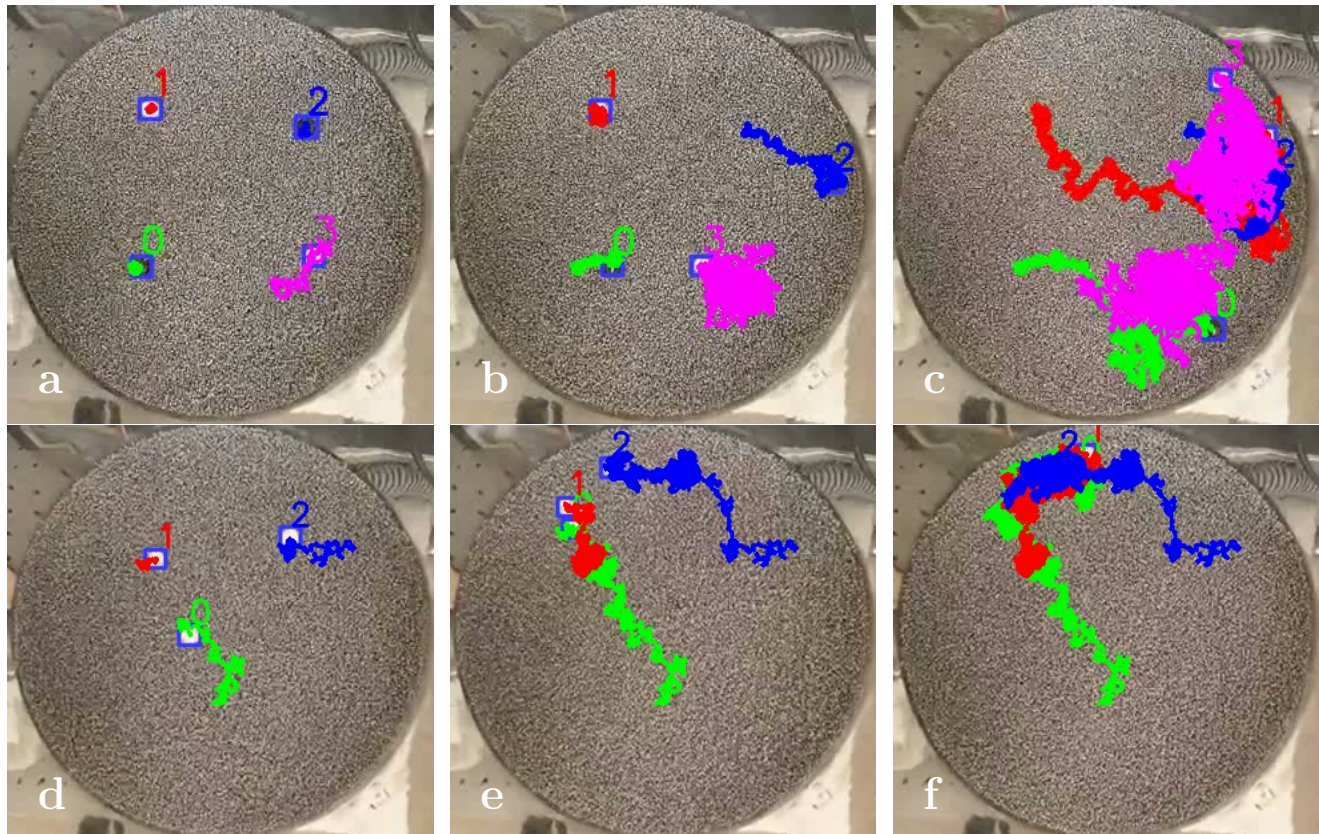


Figure 9: Real time tracking snapshots from the two white - two black (a, b, c) and two white (d, e, f) granular intruder experiments. The snapshots were taken at  $t = 17\text{s}$  for (a),  $t = 240\text{s}$  for (b),  $t = 760\text{s}$  for (c),  $t = 20\text{s}$  for (d),  $t = 180\text{s}$  for (e), and  $t = 387\text{s}$  for (e). The different colors represent the different individual intruders.

this data to explore certain characteristics of their motions under different experimental settings. Figure-10 shows the location history overlaid with the flow of the motion regarding the Control, Lights Off, Lights High, and Res Mid experiments.

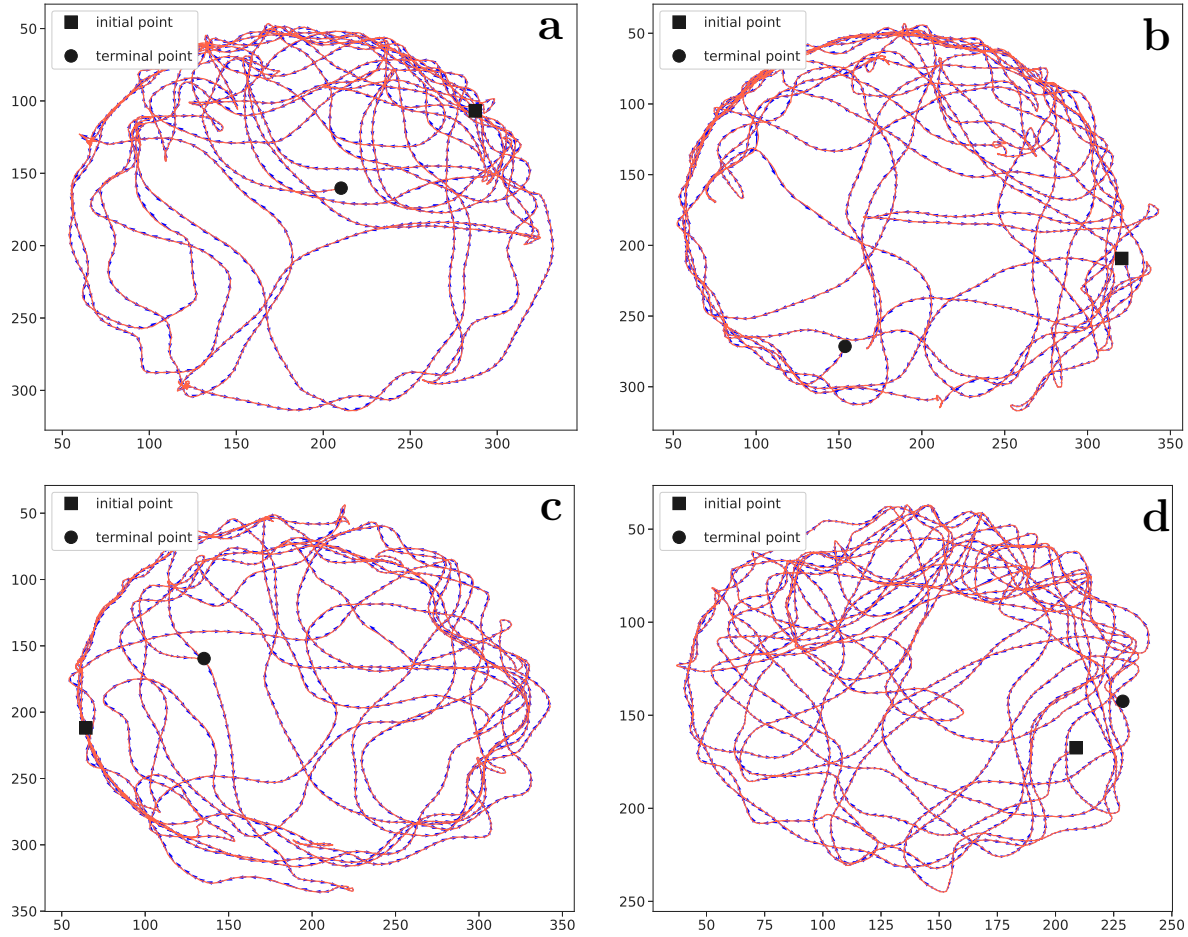


Figure 10: Full location history of the “Control” (a), “Lights Off” (b), “Lights High” (c), and “Res Mid” (d) droplet experiments. The solid (red) curves with arrows represent the trajectories of the droplets, and the square and disc (black) markers represent the initial and terminal points of the motion.

We can also inspect the average speed of the droplets calculated based on its location between two consecutive detection times and create a heatmap based on this information (see Fig-11). One can observe that the droplets in the Lights Off and Res Mid experiments are generally free from rapid accelerations. However, this is not the case for the other experiments as we observe sharp changes in speed indicated by the colorbar.

In the Faraday experiment which was carried out above the Faraday threshold, one can visually confirm that the droplet motion occurs in the vicinity of its initial location. As seen in Fig-12, the walker bounces back and forth between certain locations. Relatively sparse and discrete red points surrounded by blue points indicate sharp speed changes (potentially sharp turns) at these locations.

Similarly, we can inspect the speed map for the individual intruders in flow experiments. Our results can be seen in Fig-13 and Fig-14. We observe that the motion of the intruders is generally free from rapid distortions.

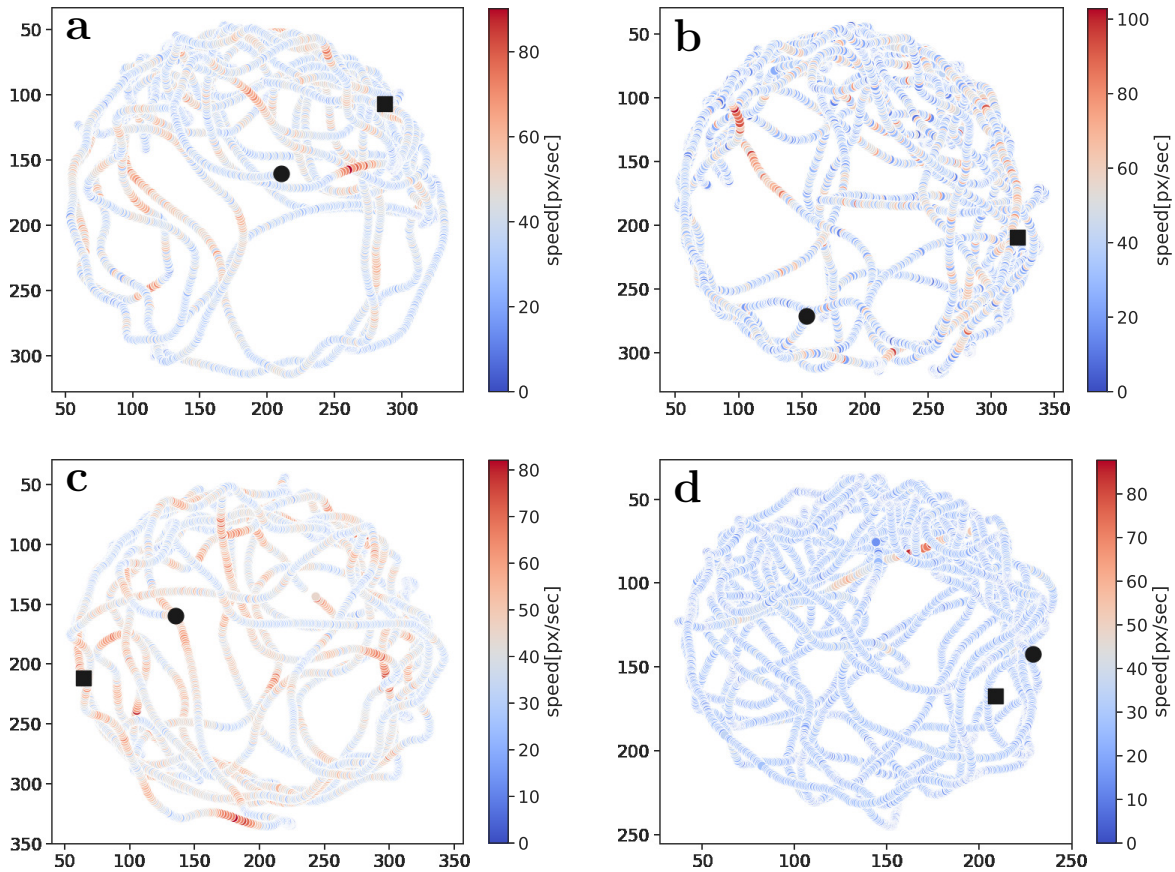


Figure 11: Speed map of the “Control” (a), “Lights Off” (b), “Lights High” (c), and “Res Mid” (d) droplet experiments. The speed of the droplet at each location (shown in Fig. 10) is represented by the color bars. The square and disc (black) markers represents the initial and terminal points of the motion.

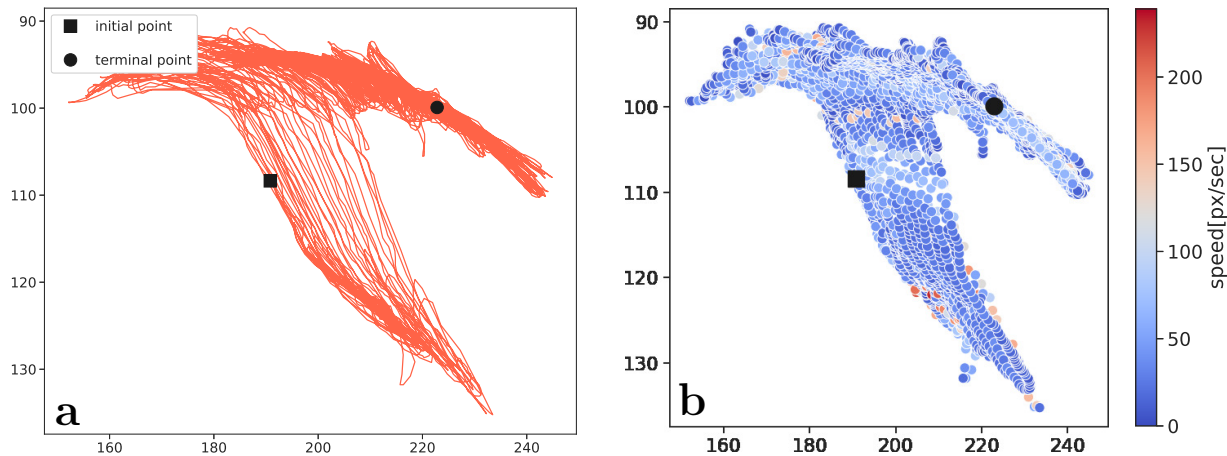


Figure 12: Location history (a) and speed map (b) for the above-threshold Faraday droplet experiment. Square and disc (black) markers represents the initial and terminal points of the motion.

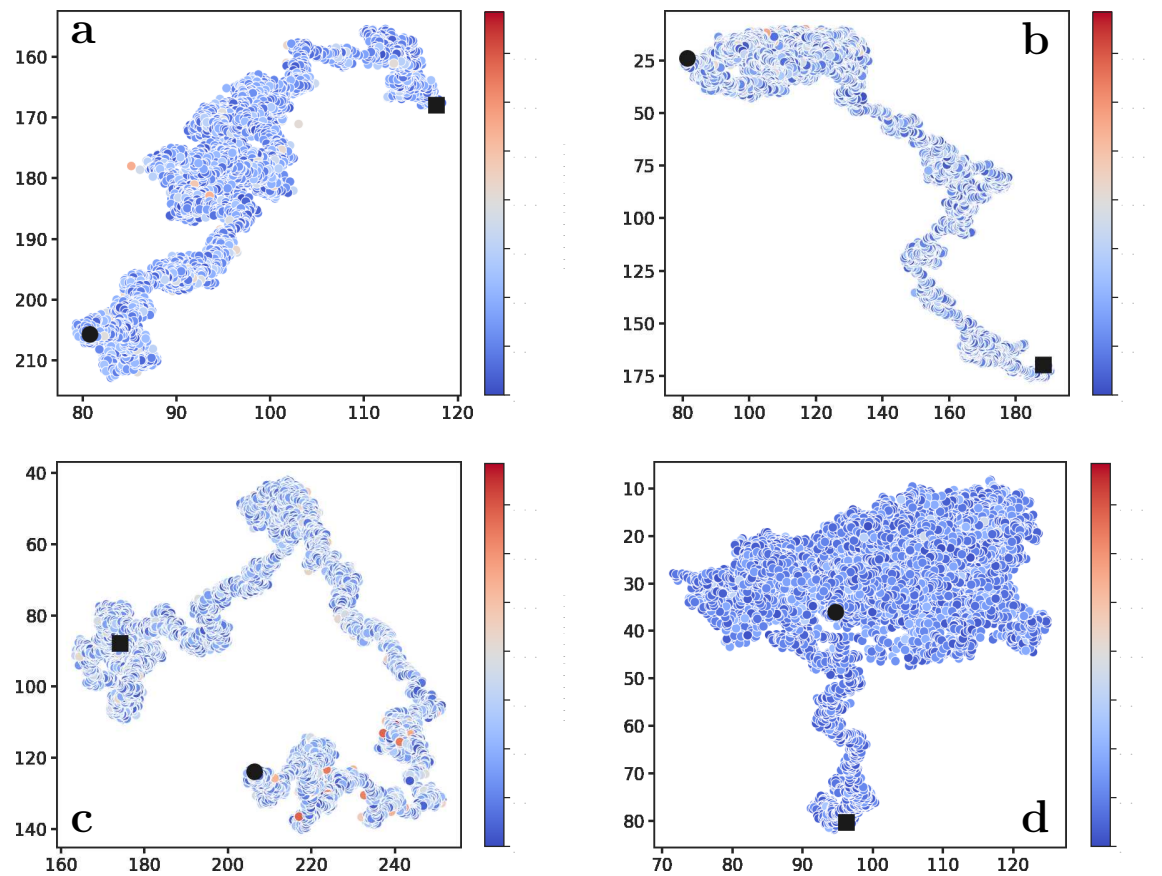


Figure 13: Speed map for granular material experiment with two black and two white intruders. **(a, b, c, d)** represent the different intruders. Square and disc (black) markers represents the initial and terminal points of the motion.

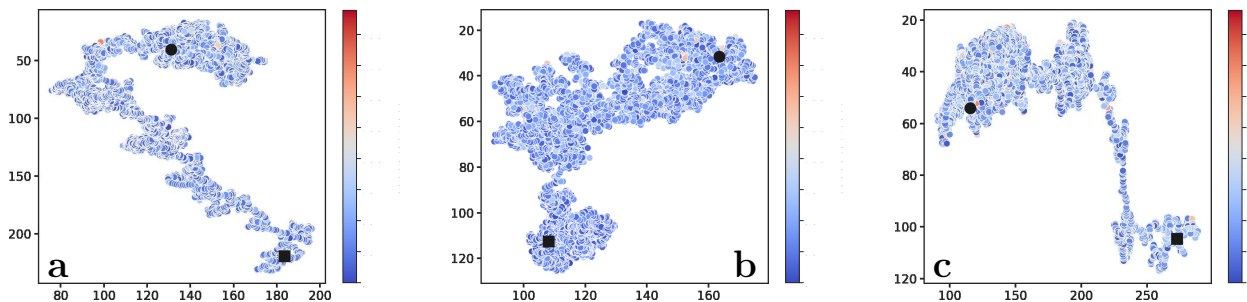


Figure 14: Speed map for granular material experiment with three white intruders. **(a, b, c)** represent the different intruders. Square and disc (black) markers represents the initial and terminal points of the motion.

#### 4.4 Comparison of the Hungarian Algorithm and StrongSORT

As detailed above, we utilize possibly the simplest approach to track individual droplets in our problem setting. To further investigate this point, we compare this simple approach with StrongSORT [82], which achieved the state-of-art performance on MOT17 and MOT20 challenges [83, 84]. StrongSORT is a detection-based tracker, i.e, it tracks the object based on *detections* provided by any object detection model. The earlier work leading to StrongSORT was proposed in the SORT (simple online and real-time tracking) method [85]. SORT utilizes a Kalman filter to predict the location of the objects in consideration and the association from one frame to next is handled by the Hungarian Algorithm. One deficiency of SORT noted is the high number of ID switches, especially during occlusion situations due to ignoring appearance information [35]. To mitigate this issue, the DeepSort method that incorporates appearance information to perform object associations between scenes is proposed in [35]. To further improve the model, DeepSort was equipped with an appearance-free link model (AFLink) to handle objects tracked in short time frames and Gaussian-smoothed interpolation(GSI) to remedy several issues associated with poor detection to produce StrongSORT [82].

We adopt the open-source Pytorch implementation of StrongSORT in [86]. Similar to our approach above, we accept a detection valid if all of the confidence scores associated with these detections are above a threshold value. This is set as 0.45 as we prescribe above to make a fair comparison. However, forcing StrongSORT to maintain exactly the same number of walkers or intruders throughout an experiment appears to break its interval method of processing tracks. Therefore, we will only impose the high confidence constraint and use it as described in the original repository.

As expected, StrongSORT successfully tracks the droplets in all single droplet experiments. However, in multiple droplet experiments, we observe that when the droplets start to interact aggressively in a close proximity, StrongSORT suffers from multiple ID switches. To support this claim, we consider one 10 second segment of the Three Droplet experiment where the droplets are closely interacting with each other. We first annotated the frames corresponding to this time window to obtain the ground truth trajectories of each individual droplet. We then separately obtained tracking results for both the Hungarian Algorithm and StrongSORT.

In Fig.-15, the background image is the very last frame of the approximately 10 second video segment. The top and bottom figures show the trajectories of two different droplets. Green discs and squares mark the initial and terminal points of the corresponding ground truth trajectory, respectively. Thus, the droplet in consideration overlaps with the green square marker. The figures on the left column display the trajectories obtained via the Hungarian Algorithm while figures on the right column display the StrongSORT trajectories, both of which are overlaid on the ground-truth trajectories. Due to an ID switch, StrongSORT fails to track the corresponding droplet and its trajectories end up at the wrong droplet ID by the end of the video segment.

We should carefully note that these ID switches occur multiple times for both the Two Droplets and Three Droplets experiments. One ID switch for each of the Three Droplets and Two Droplets experiments in two consecutive frames is depicted in Fig-16. In each case, StrongSORT was initially capable of tracking each walker. However, it fails to do so in some scenes where droplets are significantly closer to each other than in earlier frames, which were successfully tracked. We have not observed any ID switch when the distance between droplets is of moderate level and not all close contact moments result in ID switch as well.

It appears that one reason why StrongSORT suffers from ID switches in multiple droplet experiments is the nonlinear motion of walkers between successive scenes combined with almost identical appearances. The former case is not actually present in granular flow experiments in the sense that the displacement of intruders between two successive frames is significantly smaller than what we observe in droplet experiments. Yet, in granular flow, StrongSORT fails to track intruders in the 2black2white experiment multiple

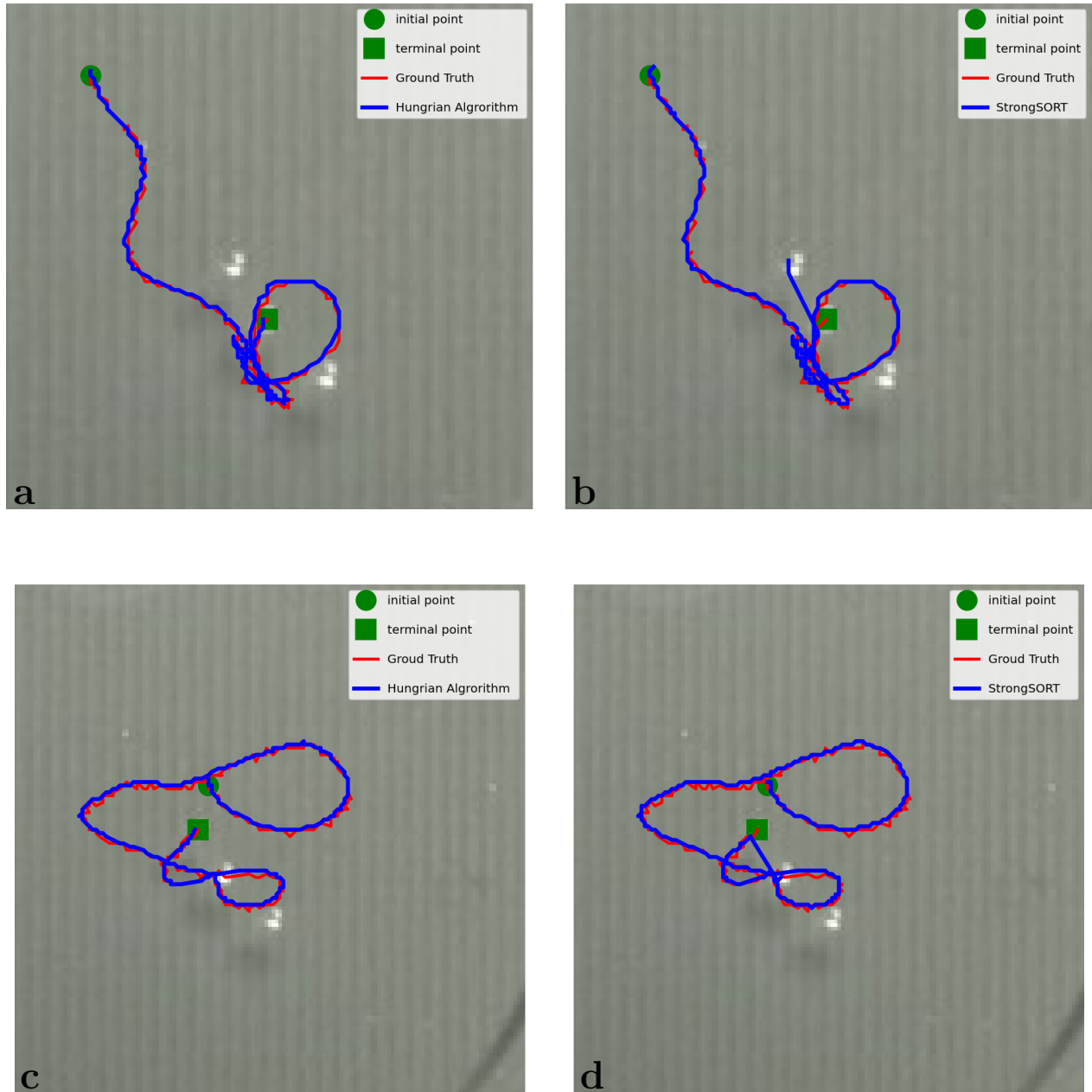


Figure 15: Ground-truth trajectories compared to trajectories produced by both the Hungarian Algorithm (a, c) and StrongSORT (b, d). (a, b) represent the first droplet, and (c, d) represent the second droplet.

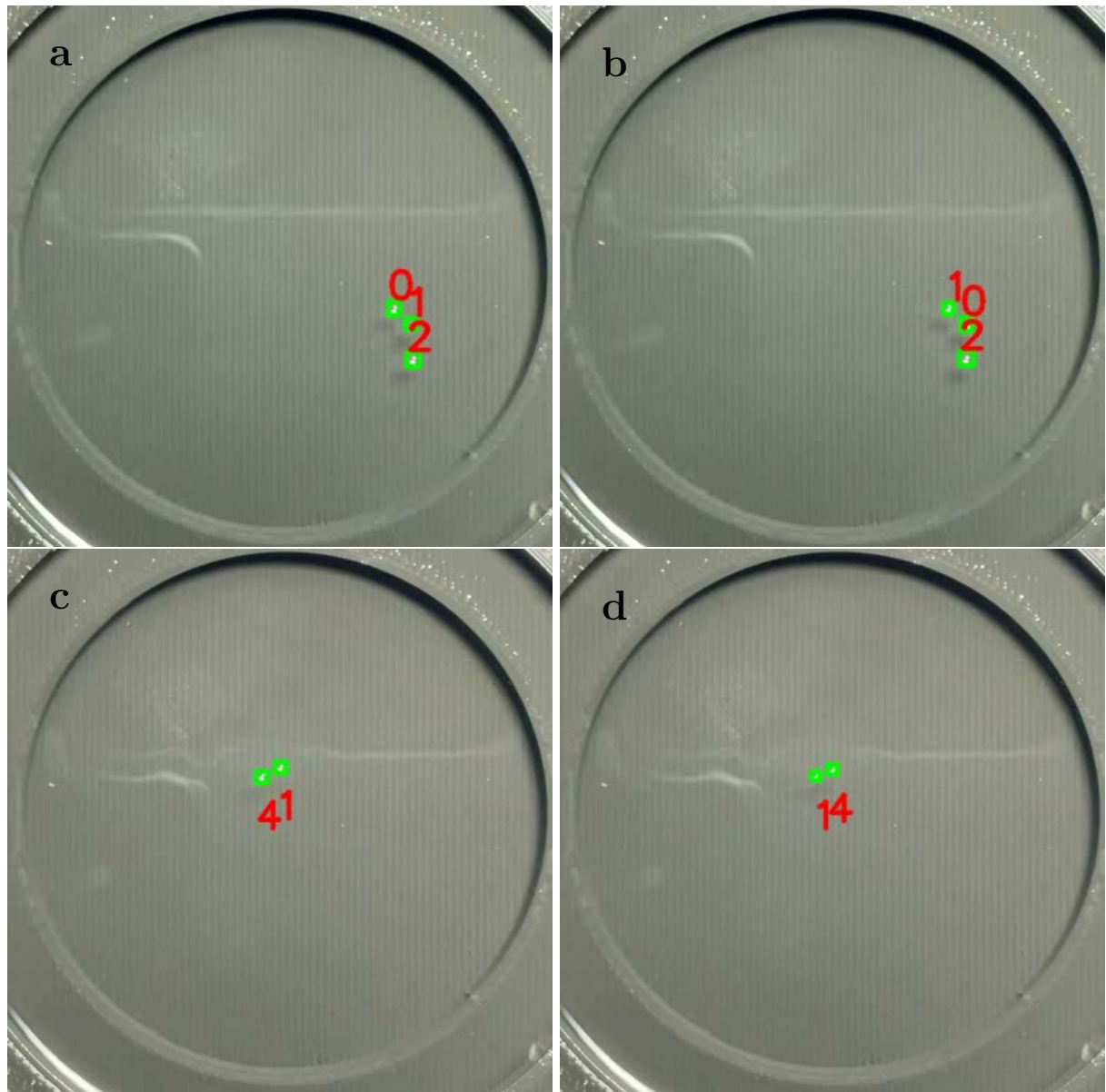


Figure 16: ID switches by StrongSORT in the Three Droplets experiment (a, b) and the Two Droplets experiment (c, d), where (a, c) and (b, d) represent two consecutive frames.

times (see Fig-17) and it fails once in the 3white experiment (see Fig-18). In these figures, the top rows display two successive frames where StrongSORT fails to maintain the same IDs for intruders. The second row in each figure shows the same scenes tracked by the Hungarian Algorithm which successfully maintains the same IDs.

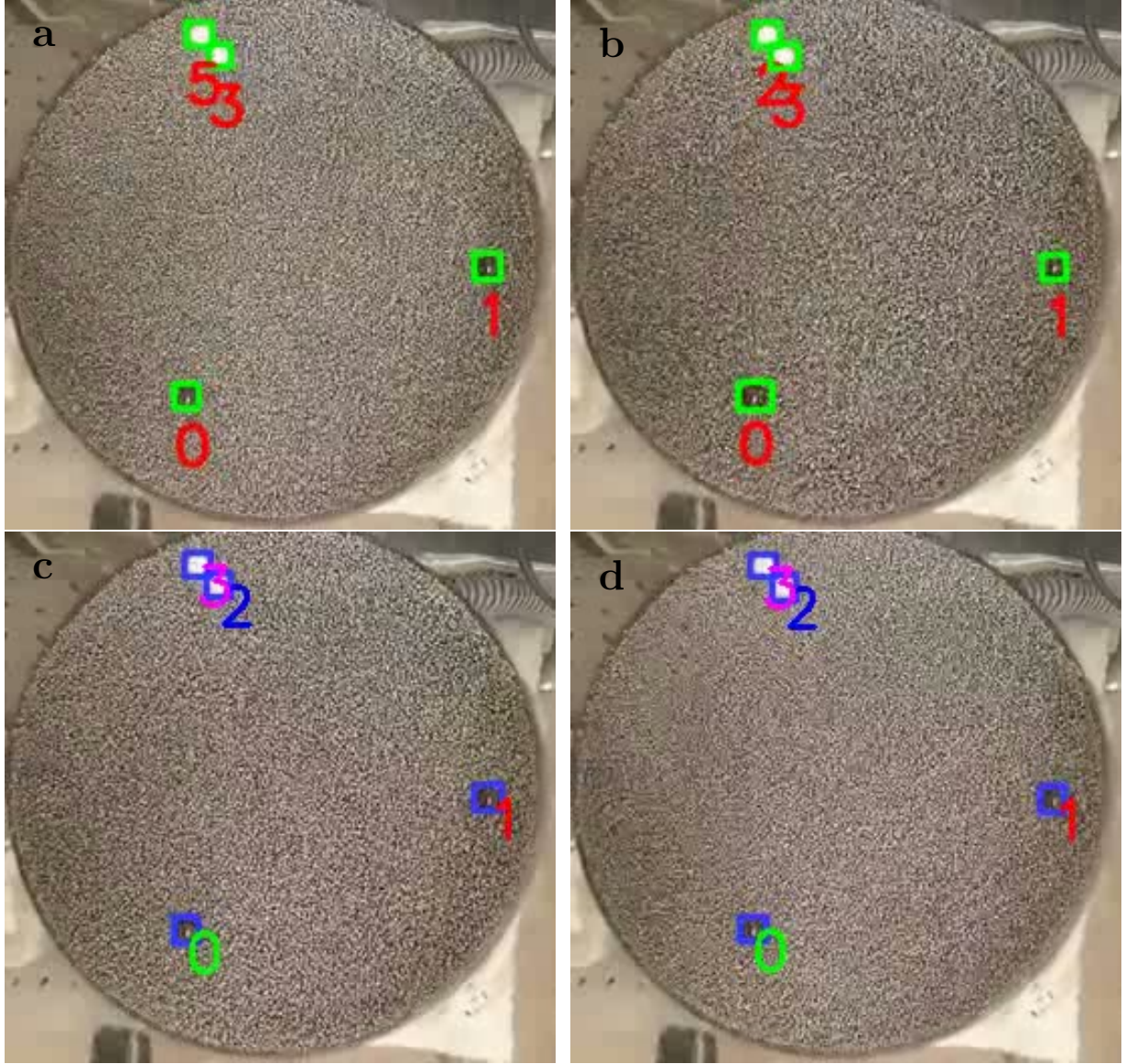


Figure 17: ID switch in the granular material experiments with two black and two white intruders by StrongSORT (a, b), and a lack thereof by the Hungarian Algorithm (c, d), where (a, c) and (b, d) represent two consecutive frames.

Results in this section demonstrate that one should be cautious prior to employing a state-of-the-art tracker to extract the trajectories in wave-particle entities experiments. The black-box nature of those methods may be particularly problematic. While our simple distance-based Hungarian Algorithm approach is free of ID switches in all experiments, StrongSORT fails on numerous occasions for experiments carried out with multiple wave-particle entities despite the fact StrongSORT draws upon the Hungarian algorithm. As noted above, it is nontrivial to identify the source of this failure due to the black-box

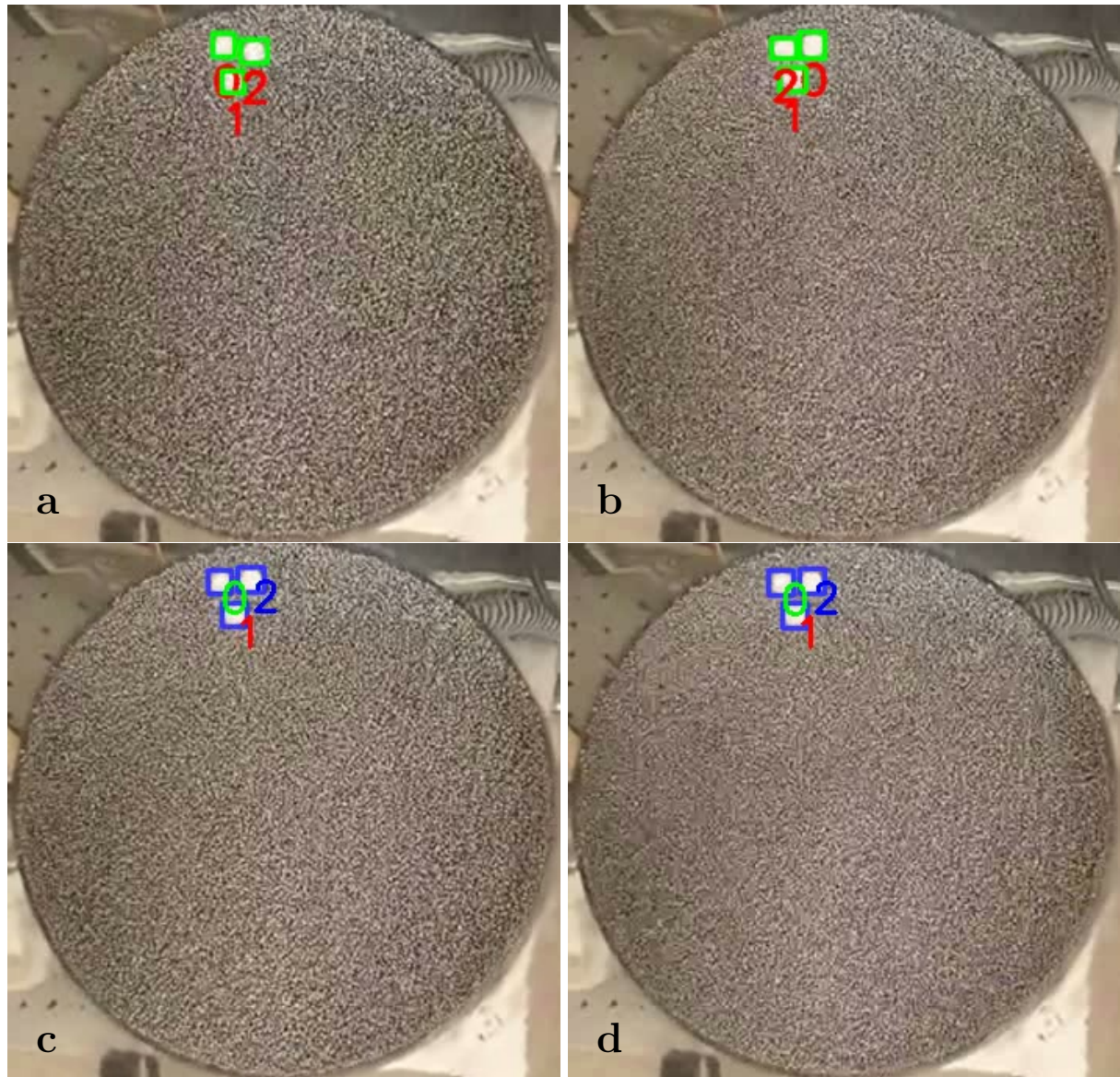


Figure 18: ID switch in the granular material experiments with three white intruders by StrongSORT (a, b), and a lack thereof by the Hungarian Algorithm (c, d), where (a, c) and (b, d) represent two consecutive frames.

nature of StrongSORT. Based on the high detection rates accomplished by YOLO, our tracking approach is interpretable in the context of our experiments. Assuming we have similar detection rates with Table-6 and Table-7, any ID switch in our approach would most likely be caused by large displacements of wave-particle entities between two successive detections as we avoid relying on motion-predictor or feature-extractor for tracking. Recording experiments at a higher frame rate would assist our tracking algorithm in better resolving the motion of wave-particle entities. We demonstrated this approach and the viability of YOLOv5 given higher frame rates on the White Corral experiment captured at 60 fps. A similar method may be applied to correct any potential ID switch that may occur with our tracking algorithm.

We lastly note that one can attempt to programmatically identify each ID switch in StrongSORT and correct the trajectories accordingly. However, this is intractable due to various reasons. While it may be possible to verify whether a new ID has been created or an existing one has been lost, it is unfeasible to *correct* ID switches in real time for experiments with multiple objects, since object IDs are simply a group of integers without any specific structure. Otherwise, the issues of ID switching in multi-object detection problems would be nonexistent. As noted above, an ID switch usually occurs when multiple objects are in close proximity to each other. Thus, correcting misidentifications by inspecting jumps in location due to ID switches is not a feasible attempt. It is important to keep in mind that the difficulty of this attempt increases in proportion to both the duration of the experiment and the number of objects that need to be tracked.

## 5 Conclusion and Future Work

We demonstrated a deep learning algorithm that enhances the object tracking pipeline for extracting the trajectories of objects of interest (i.e. walkers and intruders) in wave-particle entities experiments. Our tracking-by-detection pipeline uses YOLOv5 for detection and the Hungarian Algorithm for tracking. In a broad spectrum of the walking droplet and granular intruder experiments, the proposed method identifies the individual walkers and intruders with near-perfect detection accuracy and tracks them over the course of the experiment without any identity switches. Trajectory extraction thereby enables the examination of important characteristics hidden in the dynamics of the wave-particle entities.

One of the major goals of this work is to promote data-driven discovery of underlying physics governing the motion of wave-particle entities in classical experiments. An essential component of these efforts is to accurately extract the dynamics in a broad spectrum of experimental settings and to significantly automatize this process. One can then create a vast amount of rich data to serve as a testing and exploration ground for understanding these experiments. Of particular importance is understanding the resulting dynamics that emerge in  $N$ -particle systems driven by wave-particle dynamics.

Our future work regarding this study is twofold. As demonstrated in several figures above, wave-particle entities usually exhibit a complex trajectory. Therefore, we are unlikely to describe the full motion of these entities with a single set of governing equations. However, our preliminary results indicate that it could be possible to identify the governing dynamics in short patches using the sparse regression method SINDY [87]. This will constitute the first direction of our future work. The second direction is to investigate the existence of spatio-temporal modes which dominate the evolution of the system. This investigation is based on the hypothesis that the dynamics of this high-dimensional dataset may be described by underlying lower-dimensional patterns. To uncover these patterns, we will investigate several modal decomposition techniques such as proper orthogonal decomposition [88] and dynamic mode decomposition (DMD) [89, 90].

The codes, datasets, and results of this study will be made available in a public repository to promote scientific discovery in this field. Our GitHub repository offers further information for readers [91]. Moreover, we provide detailed step-by-step tutorial on how to adopt our repository for similar problem

domains.

The method presented in this manuscript will resolve numerous issues concerning tracking the long-time trajectory statistics of wave-particle entities. Even small discrepancies at inopportune times can accumulate to produce incorrect scientific results. Our present pipeline is robust across variations in experimental settings and across complex interactions among several wave-particle entities. We foresee that an improvement in the accuracy of observations will lead to better reproducibility and more transparency in experimental studies.

## Appendix A: Conventional Detection Methods

In this section we detail the results of alternative detection methods performed on the walking droplet experiments. Specifically, we compare and contrast the performance of image processing, background subtraction, and the Viola-Jones methods under various experimental conditions. All of these methods, while more simplistic in nature than YOLOv5, come with drawbacks and can fail in some conditions.

### A.1 Image Processing

Image processing algorithms apply operations or filters to images in order to extract meaningful information. In general, image processing algorithms do not need to be trained but do require a few parameters to be tuned for each experiment. Their simplicity comes at a cost, however. Most of the image processing methods suffer heavily from noise in the image and experimental setup. One procedure stood above the rest with optimistic results. The combination of edge detection and Hough transform, after parameter tuning, reported high precision and recall on all videos except Res Mid and Faraday. This inconsistency is the trade off made when applying image processing algorithms in exchange for ease of use.

#### A.1.1 Hough Transform

The simplest of the image processing algorithms we applied is arguably the Hough transform. In Hough transform, shapes in the pixels of an image are identified through a voting procedure. This technique has been shown to detect circles within an image [38, 39, 40]. As our droplets appear mostly circular in the videos we captured, we will apply the Hough transform as a last step to all our image processing methods. We implement the Hough transform for circle detection by utilizing the built-in *imfindcircles* function in MATLAB. Using parameters *RadiusRange* = [2, 5], *Sensitivity* = 0.95, and *EdgeThreshold* = 0.15 on the Control video, we obtained a recall of 0.98 and a precision of 0.48 within the corral region out of 50 frames throughout the video. We ignore false positives outside the corral region since we can safely assume droplets never escape the corral region. The parameters we chose maximized recall but introduced many false positives and therefore a low precision. Using parameters *RadiusRange* = [2, 5], *Sensitivity* = 0.96, *EdgeThreshold* = 0.1 on the Lights Off video, we obtained a recall of 1.00 and a precision of 0.93, which is an improvement over the control setup as much of the noise and imperfections in the background are no longer visible. However, there still remain a significant number of false positives. Having additional droplets do not seem to decrease the performance of the Hough Transform. In contrast, both lower resolution droplets and a white corral background decimate the performance. Perhaps unsurprisingly, the Hough Transform completely fails when detecting droplets in the Faraday video as the Faraday waves in the background produce too many false positives regardless of the parameters used. It is also important to note that in all of the cases, the region outside of the corral produced many false positives due to imperfections in the 3D printed corral which were not counted. Frames showing detections in various experimental conditions can be seen in Figure 19. Table 8 lists the results from the Hough Transform experiment.

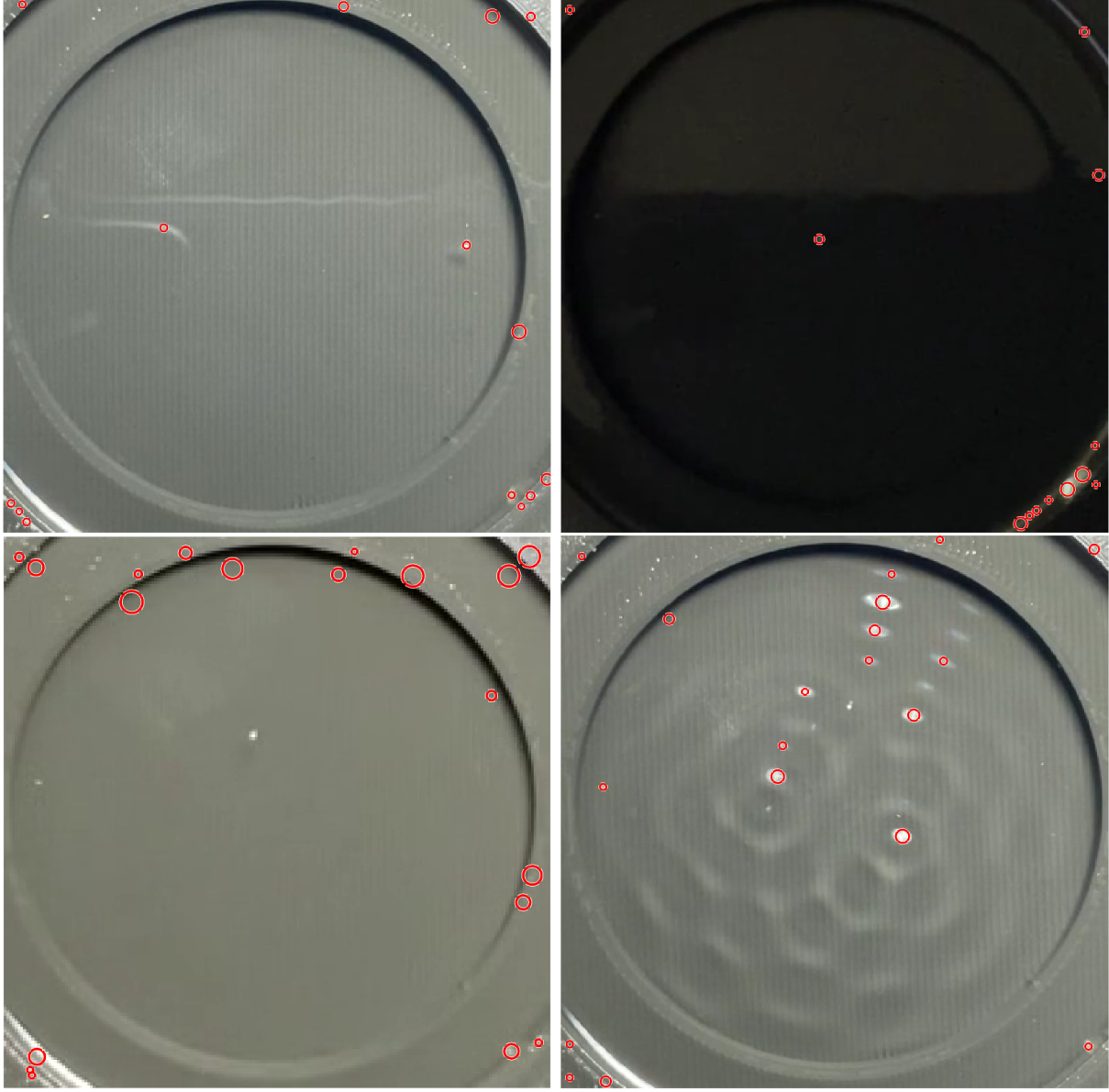


Figure 19: The upper left image shows a frame in the control video. In this frame, the droplet to the right of the corral is correctly detected but there is another false positive detection made within the corral region. Additionally, the imperfection to the left of the corral is at times mistaken for a droplet as well. The upper right image shows the Lights Off video, the lower left image shows the Res Low video, and the lower right image shows the Faraday video.

#### A.1.2 Top-Hat Transform

One additional step we included to improve image processing performance was carrying out morphological operations prior to applying the Hough Transform. We applied the top-hat transform to reduce uneven lighting and to enhance the droplet shapes against the background [41]. The top-hat transform computes and subtracts the morphological opening of an image from itself. Figure 20 shows the results of the transform. The performance of the top-hat transform can be seen in Table 9. Overall, the inclusion of the top-hat transform significantly improved precision while keeping recall about the same (and in the case of

Table 8: Hough Transform Results

Experiment	RadiusRange	Sensitivity	EdgeThreshold	Recall	Precision
Control	[2 5]	0.95	0.15	0.98	0.48
Lights Off	[2 5]	0.96	0.1	1.00	0.93
Lights Low	[2 5]	0.95	0.15	0.98	0.74
Lights High	[2 5]	0.95	0.15	0.96	0.40
Two Droplets	[2 5]	0.95	0.15	0.98	0.66
Three Droplets	[2 5]	0.95	0.15	0.97	0.87
Res Low	[1 4]	0.95	0.12	0.58	0.17
Res Mid	[2 5]	0.955	0.1	0.88	0.43
Faraday	X	X	X	X	X
Corral White	[2 5]	0.95	0.25	0.46	0.49

the Res Low video both recall and precision were improved). However, the detection is still not perfect, failing when applied to the Faraday video and performing poorly on the Corral White video. Additionally, precision is generally low under extreme lighting (Lights Low and Lights High) and lower resolutions (Res Low and Res Mid).

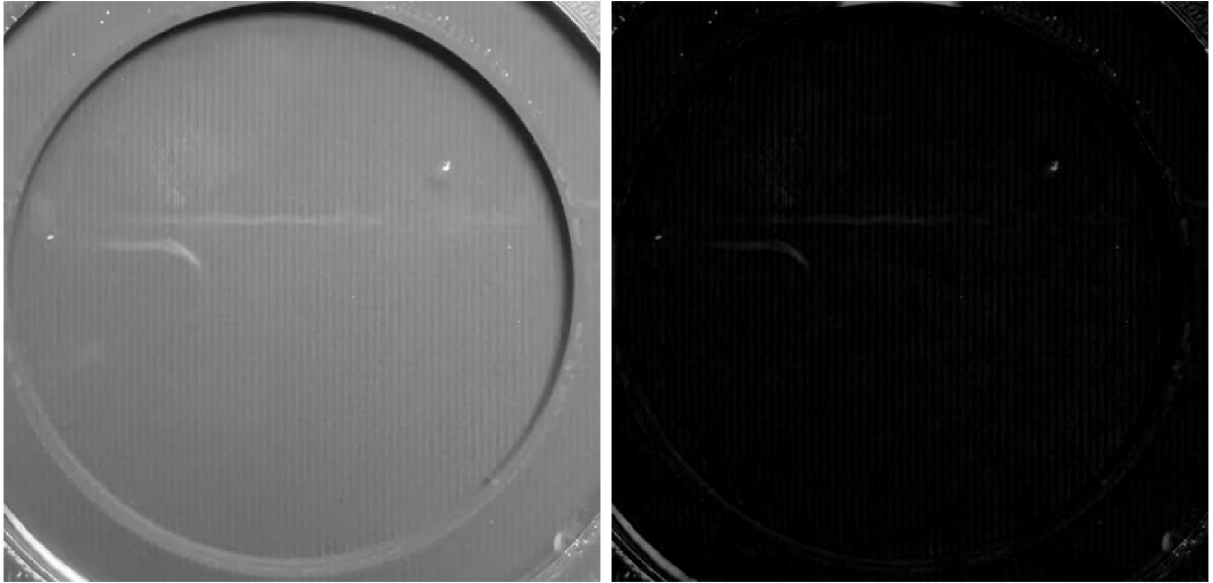


Figure 20: Before (left) and after (right) top-hat transform

### A.1.3 Edge Detection

We also experimented with applying edge detection before using *imfindcircles*. MATLAB already maintains a built-in *edge* function that we utilized [42]. After experimenting with available methods, we noted that the Canny method generally outperformed others at ignoring noise and imperfections within the image (see Figure 21). The Canny edge detection method is a multi-stage process that incorporates filters and thresholding to make accurate and reliable edge detections [43]. Again, the performance of edge detection is listed below in Table 10. Incorporating edge detection resulted in a improved performances compared to using the top-hat transform. This procedure only had trouble with the Res Mid and Corral

Table 9: Top-Hat Filtering Results

Experiment	THRadius	RadiusRange	Sensitivity	EdgeThreshold	Recall	Precision
Control	5	[2 5]	0.95	0.2	0.94	0.92
Lights Off	5	[2 5]	0.96	0.2	1.00	1.00
Lights Low	5	[2 5]	0.95	0.2	0.98	0.82
Lights High	5	[2 5]	0.95	0.2	0.94	0.87
Two Droplets	5	[2 5]	0.95	0.2	0.95	0.92
Three Droplets	5	[2 5]	0.95	0.2	0.95	0.96
Res Low	5	[1 4]	0.96	0.2	0.96	0.76
Res Mid	5	[2 5]	0.955	0.2	0.88	0.86
Faraday	X	X	X	X	X	X
Corral White	5	[2 5]	0.94	0.2	0.38	0.40

White videos. Note that having a score of 1.00 does not mean perfect detections as only 50 frames were considered in calculating the recall and precision. For example, the Three Droplets video produced false negatives despite having a 1.00 recall. Unfortunately, the Canny method still falls short of making accurate detections on the Faraday video as it is difficult to distinguish Faraday waves from droplets by simply examining edges and circles. While a potentially viable method in controlled experimental conditions, using edge detection may not be the most robust as it dips in performance for the Res Mid video but reported good performances for higher and lower resolutions.

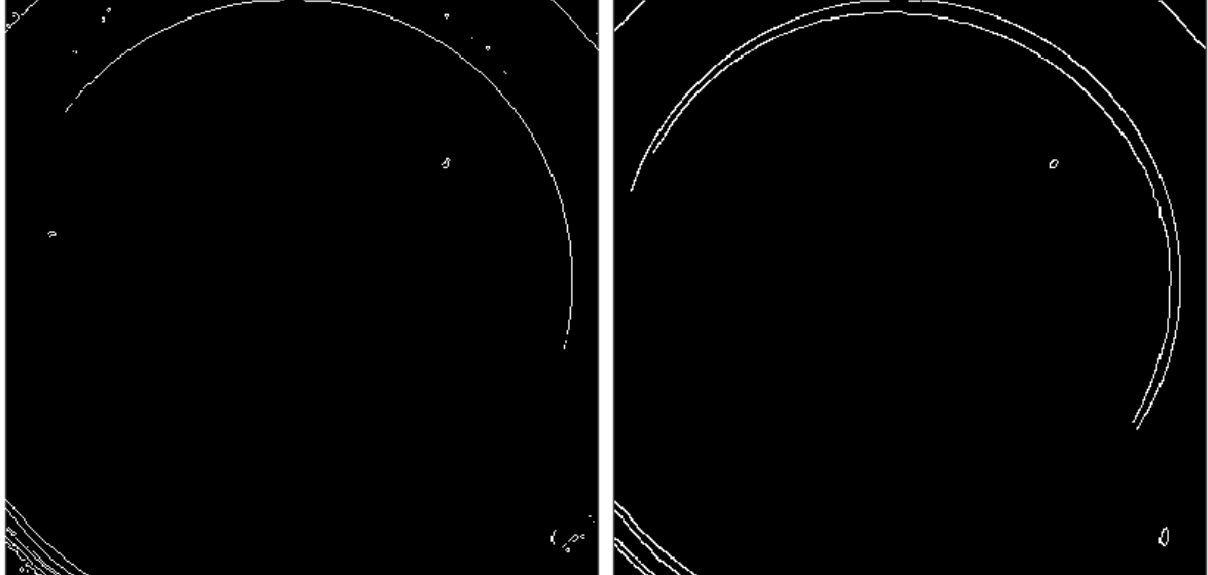


Figure 21: The default Sobel method in MATLAB (left) picks up on the corral imperfections while the Canny method (right) is able to filter out such imperfections.

#### A.1.4 Watershed Transform

The last method we implemented was the watershed transform using MATLAB's built-in function *watershed*. The watershed transform segments an image into separate regions by treating the image as a topographical map [44]. Readers can see Table 11 for the results. The watershed transform produced high

Table 10: Edge Detection Results

Experiment	FudgeFactor	RadiusRange	Sensitivity	EdgeThreshold	Recall	Precision
Control	8	[2 5]	0.93	0.5	1.00	0.98
Lights Off	5	[2 5]	0.95	0.5	1.00	1.00
Lights Low	9	[2 5]	0.92	0.5	0.94	1.00
Lights High	7	[2 5]	0.92	0.5	1.00	1.00
Two Droplets	8	[2 5]	0.93	0.5	1.00	1.00
Three Droplets	8	[2 5]	0.93	0.5	1.00	1.00
Res Low	5	[1 4]	0.94	0.5	1.00	1.00
Res Mid	6	[2 5]	0.94	0.4	0.94	0.89
Faraday	X	X	X	X	X	X
Corral White	14	[2 5]	0.93	0.5	0.42	0.35

precision but was the most inconsistent algorithm so far. There is generally a low recall that varied drastically depending on the lighting level. Additionally, the watershed transform was also the only algorithm that failed completely on Res Low and Res Mid videos in addition to Faraday and Corral White videos. Figure 22 demonstrates the watershed transform in action.

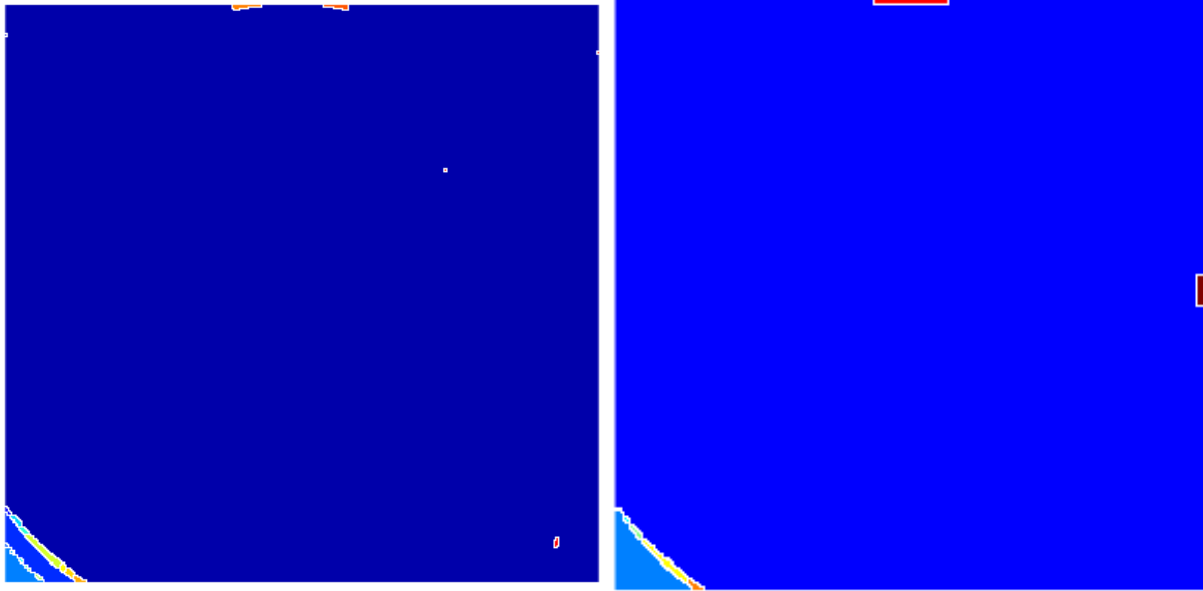


Figure 22: The watershed transform applied to the Control video (left) and the Res Mid video (right).

## A.2 Background Subtraction

Background subtraction algorithms build up a model of the static background to extract moving foreground objects in the form of a black and white foreground mask. We compared and contrasted 3 different background subtraction techniques based on Gaussian mixture models (GMM) to detect and segment the moving droplets from the similarly-colored background [45, 46]. The method MOG [47, 48] is implemented in MATLAB and MOG2 [49] and KNN [50] are both implemented in Python using the OpenCV library. For both of the Python algorithms, we first apply a threshold operation to remove any shadows from the foreground mask. Prior to detecting the droplets, we also utilize an erode then a dilate operation to

Table 11: Watershed Transform Results

Experiment	THRadius	RadiusRange	Sensitivity	EdgeThreshold	Recall	Precision
Control	5	[2 5]	0.97	0.1	0.68	1.00
Lights Off	5	[2 5]	0.97	0.1	0.3	1.00
Lights Low	5	[2 5]	0.97	0.1	0.98	1.00
Lights High	5	[2 5]	0.97	0.1	0.76	0.90
Two Droplets	5	[2 5]	0.97	0.1	0.74	1.00
Three Droplets	5	[2 5]	0.97	0.1	0.63	1.00
Res Low	X	X	X	X	X	X
Res Mid	X	X	X	X	X	X
Faraday	X	X	X	X	X	X
Corral White	X	X	X	X	X	X

remove noise from the mask (except for MOG2 and KNN when applied to the Res Low video, KNN when applied to the Res Mid video, and all algorithms when applied to the Corral White video). For the MOG algorithm implemented in MATLAB, we used 5 training frames and a training rate of 0.0001 while only detecting blobs with a minimum area of 10 (3 for Res Low and 5 for Res Mid).

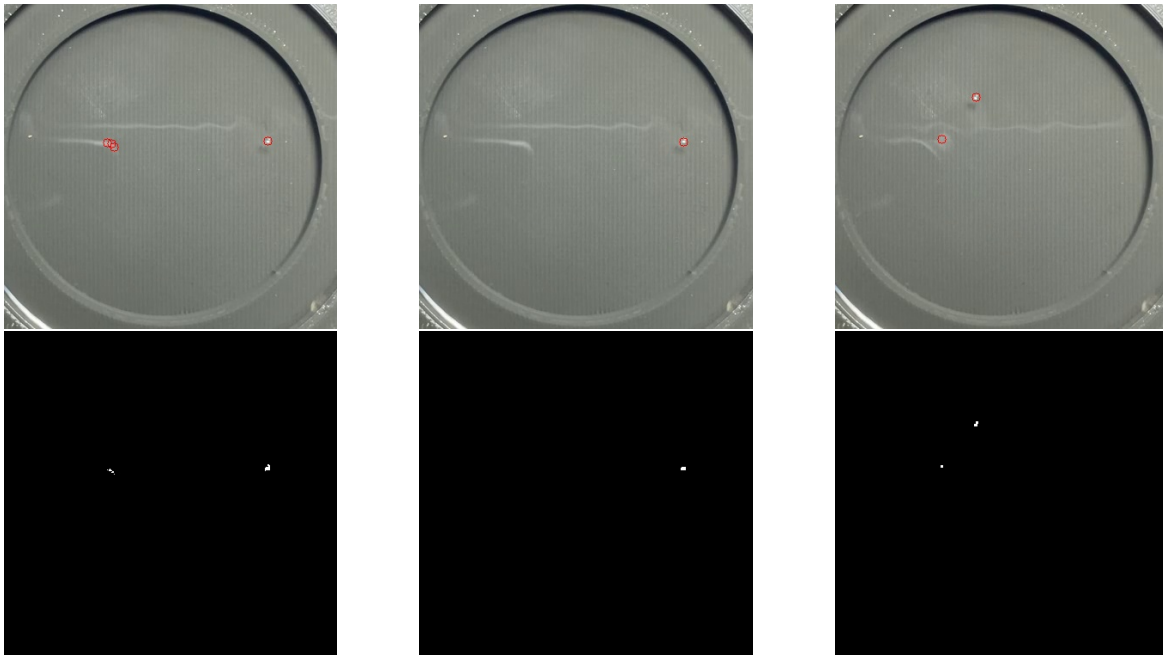


Figure 23: From left to right: frame 1 before applying erosion and dilation, frame 1 after applying erosion and dilation, and frame 2. Top images show the video post droplet detection and the bottom images show the foreground mask.

Without the erosion and dilation operations, noise within the videos translates to noise in the foreground masks which then induce false positives. We can see this in one frame (frame 1) when the KNN algorithm is applied to the Control video (as shown to the left of Figure 23). Applying the erosion and dilation operations removes most noise within the foreground mask (as shown in the middle of Figure 23). However, some noise have a large enough area such that the morphological operations are unable to remove them from the foreground mask, which then leads to false positive detections. This can be

seen in another frame (frame 2) of the same experiment (as shown to the right of Figure 23). We can potentially eliminate these false positives by increasing the number of iterations that we apply the erosion and dilation operations, but doing so will drastically decrease the recall since droplets are often erased from the foreground mask as well.

Table 12: Background Subtraction Results

Experiment	MOG (MATLAB)		MOG2 (Python)		KNN (Python)	
	Recall	Precision	Recall	Precision	Recall	Precision
Control	0.98	1.00	0.96	0.70	0.98	1.00
Lights Off	0.74	1.00	0.98	1.00	0.98	1.00
Lights Low	1.00	1.00	0.98	0.88	1.00	1.00
Lights High	0.98	0.98	1.00	0.65	1.00	1.00
Two Droplets	0.98	1.00	0.98	0.87	0.99	1.00
Three Droplets	0.99	0.99	0.97	0.88	0.99	1.00
Res Low	0.98	1.00	1.00	0.96	1.00	1.00
Res Mid	0.98	1.00	0.96	0.8	1.00	1.00
Faraday	X	X	X	X	X	X
Corral White	0.24	1.00	0.26	0.93	0.10	1.00

As expected, the motion of the Faraday waves caused all background subtraction algorithms to fail for the Faraday video. Movement in the background makes it impossible to extract the foreground based on motion. Otherwise, the KNN algorithm outperformed both MOG and MOG2 with a high recall and precision for all videos except Corral White. Again, note that having a score of 1.00 does not mean perfect detections as only 50 frames were considered in calculating the recall and precision. For example, the KNN algorithm had occasional false positive detections despite a precision score of 1.00 on most videos. While all algorithms failed to detect droplets occasionally, MOG also failed to detect droplets in a large proportion of frames for the Lights Off video. MOG2 was imprecise in general and made a significant amount of false detections in all but the Lights Off and Res Low videos. Compared to image processing techniques, background subtraction methods require less parameter tuning and do not produce false positives on 3D printing imperfections of the corral. The KNN algorithm, while not perfect, generally offers more consistency compared to image processing methods and can be viable in controlled settings. However, background subtraction algorithms do require the camera and setup to remain perfectly fixed and undisturbed throughout the experiment. Additionally, the frames of a video must be processed in chronological order.

### A.3 Viola-Jones Algorithm

The Viola-Jones Algorithm is a supervised machine learning algorithm used for object detection [53]. Supervised machine learning algorithms detect objects by training on a set of labelled training images in which rectangular bounding boxes are marked around each object of interest, and in our case droplet. We implemented the Viola-Jones Algorithm through MATLAB’s *CascadeObjectDetector* and used roughly 125 labelled training images per video and 6899 negative images [92] (although only about 250 negative samples per droplet were used by the detector at each training stage). The parameters used during training were *NumCascadeStages*, *FalseAlarmRate*, *ObjectTrainingSize*, and *FeatureType*. We kept *TruePositiveRate=0.999* the same for all videos. The results below in Table 13 were obtained by only keeping bounding boxes below an area of 200.

The Viola-Jones algorithm was designed primarily for face detection. Therefore, the low performance

Table 13: Viola-Jones Results

Experiment	Stages	FalseAlarm	TrainingSize	FeatureType	Recall	Precision
Control	6	0.02	[10 10]	LBP	0.44	1.00
Lights Off	4	0.02	[10 10]	LBP	0.42	1.00
Lights Low	4	0.01	[10 10]	LBP	0.28	0.88
Lights High	5	0.25	[10 10]	Haar	0.28	0.88
Two Droplets	4	0.2	[10 10]	Haar	0.2	0.80
Three Droplets	4	0.1	[10 10]	Haar	0.21	1.00
Res Low	X	X	X	X	X	X
Res Mid	4	0.2	[10 10]	Haar	0.28	1.00
Faraday	X	X	X	X	X	X
Corral White	X	X	X	X	X	X

is perhaps not a surprise when it comes to droplet detection. Ultimately, the minuscule, low resolution, and minimally textured droplets stand in stark contrast to highly textured faces. We obtained a low recall using the Viola-Jones algorithm for all videos and could not achieve successful detections on the Res Low, Faraday, and Corral White videos. For videos with multiple droplets, only one detection was able to be made on each frame. Although the Viola-Jones algorithm trains much faster than YOLOv5, its low performance makes it unviable as an option for droplet detection.

## Acknowledgements

The authors acknowledge support from the National Science Foundation AI Institute in Dynamic Systems (grant number 2112085). JNK further acknowledges support from the Air Force Office of Scientific Research (FA9550-19-1-0011).

## References

- [1] Y. Couder, S. Protiere, E. Fort, and A. Boudaoud. Dynamical phenomena: Walking and orbiting droplets. *Nature*, 437:208, 2005.
- [2] S. Protiere, A. Boudaoud, and Y. Couder. Particle-wave association on a fluid interface. *J. Fluid Mech.*, 554:85–108, 2006.
- [3] Y. Couder and E. Fort. Single-particle diffraction and interference at a macroscopic scale. *Phys. Rev. Lett.*, 97:154101, 2006.
- [4] J.W.M. Bush. Quantum mechanics writ large. *Proc. Nat. Acad. Sci.*, pages 1–2, 2010.
- [5] D.M. Harris, J. Moukhtar, E. Fort, Y. Couder, and J.W.M. Bush. Wavelike statistics from pilot-wave dynamics in a circular corral. *Phys. Rev. E*, 88:011001, 2013.
- [6] J.W.M. Bush. Pilot-wave hydrodynamics. *Ann. Rev. Fluid Mech.*, 49:269–292, 2015.
- [7] J.W.M. Bush. The new wave of pilot-wave theory. *Physics Today*, 68(8):47–53, 2015.
- [8] J. W. M. Bush and A. U. Oza. Hydrodynamic quantum analogs. *Reports on Progress in Physics*, 84:017001, 2021.

- [9] L. D. Tambasco, J. J. Pilgram, and J. W. M. Bush. Bouncing droplet dynamics above the faraday threshold. *Chaos*, 28:096107, 2018.
- [10] A. Rahman. Damped-driven system of bouncing droplets leading to diffusive behavior. 2022.
- [11] A. Rahman. Analyzing deterministically diffusive behavior of bouncing droplets through an energy gain-loss formulation. *To be submitted*, 2022.
- [12] E. Fort, A. Eddi, A. Boudaoud, J. Moukhtar, and Y. Couder. Path-memory induced quantization of classical orbits. *Proc. Nat. Acad. Sci.*, 107:17515, 2010.
- [13] A. Oza, D.M. Harris, R.R. Rosales, and J.W.M. Bush. Pilot-wave dynamics in a rotating frame: on the emergence of orbital quantization. *J. Fluid Mech.*, 744:404–429, 2014.
- [14] A. Oza, O. Wind-Willassen, D.M. Harris, R.R. Rosales, and J.W.M. Bush. Pilot-wave dynamics in a rotating frame: Exotic orbits. *Phys. Fluids*, 26:082101, 2014.
- [15] D.M. Harris and J.W.M. Bush. Droplets walking in a rotating frame: from quantized orbits to multimodal statistics. *J. Fluid Mech.*, 739:444–464, 2014.
- [16] L. D. Tambasco, D. M. Harris, A. U. Oza, R. R. Rosales, and J. W. M. Bush. The onset of chaos in orbital pilot-wave dynamics. *Chaos*, 26(103107), 2016.
- [17] A. U. Oza, E. Siéfert, D. M. Harris, J. Molacek, and J. W. M. Bush. Orbiting pairs of walking droplets: Dynamics and stability. *Phys. Rev. F*, 2:053601, 2017.
- [18] T. Gilet. Dynamics and statistics of wave-particle interaction in a confined geometry. *Phys. Rev. E*, 90:052917, 2014.
- [19] J. W. M. Bush, Y. Couder, T. Gilet, P. A. Milewski, and A Nachbin. Introduction to focus issue on hydrodynamic quantum analogs. *Chaos*, 28:096001, 2018.
- [20] A Rahman, Y. Joshi, and D Blackmore. Sigma map dynamics and bifurcations. *Regul. Chaotic Dyn.*, 22(6):740–749, 2017.
- [21] Aminur Rahman. Standard map-like models for single and multiple walkers in an annular cavity. *Chaos*, 28:096102, 2018.
- [22] Aminur Rahman and D. Blackmore. Interesting bifurcations in walking droplet dynamics. *Commun. Nonlinear Sci. Numer. Simul.*, 90:105348, 2020.
- [23] A. Rahman and D. Blackmore. Walking droplets through the lens of dynamical systems. *Modern Physics Letters B*, 34(34):2030009, 2020.
- [24] Thomas H. Metcalf, James B. Knight, and Heinrich M. Jaeger. Standing wave patterns in shallow beds of vibrated granular material. 236(3):202–210.
- [25] Francisco Melo, Paul Umbanhowar, and Harry L. Swinney. Transition to parametric wave patterns in a vertically oscillated granular layer. 72(1):172.
- [26] Peter Eshuis, Ko Van Der Weele, Devaraj Van Der Meer, Robert Bos, and Detlef Lohse. Phase diagram of vertically shaken granular matter. 19(12):123301.
- [27] Arshad Kudrolli. Size separation in vibrated granular matter. 67(3):209–247.

- [28] James B. Knight, E. E. Ehrichs, Vadim Yu. Kuperman, Janna K. Flint, Heinrich M. Jaeger, and Sidney R. Nagel. Experimental study of granular convection. 54(5):5726–5738.
- [29] Matthew J. Metzger, Brenda Remy, and Benjamin J. Glasser. All the brazil nuts are not on top: Vibration induced granular size segregation of binary, ternary and multi-sized mixtures. 205(1):42–51.
- [30] Sangam Srikanth, Satish Kumar Dubey, Arshad Javed, and Sanket Goel. Droplet based microfluidics integrated with machine learning. *Sensors and Actuators A: Physical*, 332:113096, 2021.
- [31] Mihir Durve, Fabio Bonaccorso, Andrea Montessori, Marco Lauricella, Adriano Tiribocchi, and Sauro Succi. A fast and efficient deep learning procedure for tracking droplet motion in dense microfluidic emulsions. *Philosophical Transactions of the Royal Society A*, 379(2208):20200400, 2021.
- [32] Mihir Durve, Adriano Tiribocchi, Fabio Bonaccorso, Andrea Montessori, Marco Lauricella, Michal Bogdan, Jan Guzowski, and Sauro Succi. Droptrack—automatic droplet tracking with yolov5 and deepsort for microfluidic applications. *Physics of Fluids*, 34(8):082003, 2022.
- [33] Mihir Durve, Fabio Bonaccorso, Andrea Montessori, Marco Lauricella, Adriano Tiribocchi, and Sauro Succi. Tracking droplets in soft granular flows with deep learning techniques. *The European Physical Journal Plus*, 136(8):864, 2021.
- [34] Glenn Jocher. ultralytics/yolov5: v3.1 - Bug Fixes and Performance Improvements. <https://github.com/ultralytics/yolov5>, October 2020.
- [35] Nicolai Wojke, Alex Bewley, and Dietrich Paulus. Simple online and realtime tracking with a deep association metric. In *2017 IEEE international conference on image processing (ICIP)*, pages 3645–3649. IEEE, 2017.
- [36] Gregory Philip Rutkowski, Ilgar Azizov, Evan Unmann, Marcin Dudek, and Brian Arthur Grimes. Microfluidic droplet detection via region-based and single-pass convolutional neural networks with comparison to conventional image analysis methodologies. *Machine Learning with Applications*, 7:100222, 2022.
- [37] Shaoqing Ren, Kaiming He, Ross Girshick, and Jian Sun. Faster r-cnn: Towards real-time object detection with region proposal networks. *Advances in neural information processing systems*, 28, 2015.
- [38] Richard O. Duda and Peter E. Hart. Use of the hough transformation to detect lines and curves in pictures. *Commun. ACM*, 15(1):11–15, jan 1972.
- [39] HK Yuen, J Princen, J Illingworth, and J Kittler. Comparative study of hough transform methods for circle finding. *Image and Vision Computing*, 8(1):71–77, 1990.
- [40] T.J. Atherton and D.J. Kerbyson. Size invariant circle detection. *Image and Vision Computing*, 17(11):795–803, 1999.
- [41] Suman Thapar and Shevani Garg. Study and implementation of various morphology based image contrast enhancement techniques. *Int. J. Comput. Bus. Res.*, 128:2229–6166, 2012.
- [42] MathWorks. Find edges in 2-D grayscale image - MATLAB edge, 2011.
- [43] John Canny. A computational approach to edge detection. *IEEE Transactions on Pattern Analysis and Machine Intelligence*, PAMI-8(6):679–698, 1986.

- [44] Fernand Meyer. Topographic distance and watershed lines. *Signal Processing*, 38(1):113–125, 1994. Mathematical Morphology and its Applications to Signal Processing.
- [45] Nir Friedman and Stuart Russell. Image segmentation in video sequences: A probabilistic approach, 2013.
- [46] Imane Benraya and Nadjia Benblidia. Comparison of background subtraction methods. In *2018 International Conference on Applied Smart Systems (ICASS)*, pages 1–5, 2018.
- [47] C. Stauffer and W. Eric L. Grimson. Adaptive background mixture models for real-time tracking. *Proceedings. 1999 IEEE Computer Society Conference on Computer Vision and Pattern Recognition (Cat. No PR00149)*, 2:246–252 Vol. 2, 1999.
- [48] Pakorn KaewTrakulPong and R. Bowden. An improved adaptive background mixture model for realtime tracking with shadow detection. 2002.
- [49] Z. Zivkovic. Improved adaptive gaussian mixture model for background subtraction. In *Proceedings of the 17th International Conference on Pattern Recognition, 2004. ICPR 2004.*, volume 2, pages 28–31 Vol.2, 2004.
- [50] Zoran Zivkovic and Ferdinand van der Heijden. Efficient adaptive density estimation per image pixel for the task of background subtraction. *Pattern Recognition Letters*, 27(7):773–780, 2006.
- [51] Jacob Grosek and J Nathan Kutz. Dynamic mode decomposition for real-time background/foreground separation in video. *arXiv preprint arXiv:1404.7592*, 2014.
- [52] N Benjamin Erichson, Steven L Brunton, and J Nathan Kutz. Compressed dynamic mode decomposition for background modeling. *Journal of Real-Time Image Processing*, 16(5):1479–1492, 2019.
- [53] P. Viola and M. Jones. Rapid object detection using a boosted cascade of simple features. In *Proceedings of the 2001 IEEE Computer Society Conference on Computer Vision and Pattern Recognition. CVPR 2001*, volume 1, pages I–I, 2001.
- [54] I. Seginer, R. Elster, J. Goodrum, and M. Rieger. Plant wilt detection by computer-vision tracking of leaf tips. *Transactions of the ASAE*, 35(5):1563–1567, 1992.
- [55] Peter W. Sites and Michael J. Delwiche. Computer vision to locate fruit on a tree. *Transactions of the ASAE*, 31(1):257–265, 1988.
- [56] Shuo Zhu, Chunxu Li, James Rogers, Mario Gianni, and Ian Howard. A real-time double emulsion droplets detection system using hough circle transform and color detection. In *2021 27th International Conference on Mechatronics and Machine Vision in Practice (M2VIP)*, pages 36–41, 2021.
- [57] S. Kulju, L. Riegger, P. Koltay, K. Mattila, and J. Hyväläluoma. Fluid flow simulations meet high-speed video: Computer vision comparison of droplet dynamics. *Journal of Colloid and Interface Science*, 522:48–56, 2018.
- [58] Haifeng Zhao, Jun Zhou, Yanyang Gu, Chee Meng Benjamin Ho, Say Hwa Tan, and Yongsheng Gao. Real- time computing for droplet detection and recognition. In *2018 IEEE International Conference on Real-time Computing and Robotics (RCAR)*, pages 589–594, 2018.
- [59] Z.Z. Chong, S.B. Tor, Gañán-Calvo, and A.M. Automated droplet measurement (adm): an enhanced video processing software for rapid droplet measurements. *Microfluidics Nanofluidics*, 2016.

- [60] Akash D. Nakarmi, Lie Tang, and Hongwei Xin. Automated tracking and behavior quantification of laying hens using 3d computer vision and radio frequency identification technologies. *Transactions of the ASABE*, 2014.
- [61] Malika Nisal Ratnayake, Adrian G. Dyer, and Alan Dorin. Tracking individual honeybees among wildflower clusters with computer vision-facilitated pollinator monitoring. *PLOS ONE*, 16(2):1–20, 02 2021.
- [62] Kang Li, Eric D. Miller, Mei Chen, Takeo Kanade, Lee E. Weiss, and Phil G. Campbell. Computer vision tracking of stemness. In *2008 5th IEEE International Symposium on Biomedical Imaging: From Nano to Macro*, pages 847–850, 2008.
- [63] Richard Szeliski. *Computer vision: algorithms and applications*. Springer Nature, 2022.
- [64] David Forsyth and Jean Ponce. *Computer Vision: A Modern Approach. (Second edition)*. Prentice Hall, November 2011.
- [65] A. Rosenfeld. Computer vision: basic principles. *Proceedings of the IEEE*, 76(8):863–868, 1988.
- [66] Syed Sahil Abbas Zaidi, Mohammad Samar Ansari, Asra Aslam, Nadia Kanwal, Mamoona Asghar, and Brian Lee. A survey of modern deep learning based object detection models. *Digital Signal Processing*, page 103514, 2022.
- [67] Li Liu, Wanli Ouyang, Xiaogang Wang, Paul Fieguth, Jie Chen, Xinwang Liu, and Matti Pietikäinen. Deep learning for generic object detection: A survey. *International journal of computer vision*, 128(2):261–318, 2020.
- [68] Joseph Redmon, Santosh Divvala, Ross Girshick, and Ali Farhadi. You only look once: Unified, real-time object detection. In *Proceedings of the IEEE conference on computer vision and pattern recognition*, pages 779–788, 2016.
- [69] Joseph Redmon and Ali Farhadi. Yolo9000: better, faster, stronger. In *Proceedings of the IEEE conference on computer vision and pattern recognition*, pages 7263–7271, 2017.
- [70] Joseph Redmon and Ali Farhadi. Yolov3: An incremental improvement. *arXiv preprint arXiv:1804.02767*, 2018.
- [71] Alexey Bochkovskiy, Chien-Yao Wang, and Hong-Yuan Mark Liao. Yolov4: Optimal speed and accuracy of object detection. *arXiv preprint arXiv:2004.10934*, 2020.
- [72] Tsung-Yi Lin, Michael Maire, Serge Belongie, James Hays, Pietro Perona, Deva Ramanan, Piotr Dollár, and C Lawrence Zitnick. Microsoft coco: Common objects in context. In *European conference on computer vision*, pages 740–755. Springer, 2014.
- [73] Mark Everingham, Luc Van Gool, Christopher KI Williams, John Winn, and Andrew Zisserman. The pascal visual object classes (voc) challenge. *International journal of computer vision*, 88(2):303–338, 2010.
- [74] Tzutalin. Labelimg. Free Software: MIT License, 2015.
- [75] Adam Paszke, Sam Gross, Francisco Massa, Adam Lerer, James Bradbury, Gregory Chanan, Trevor Killeen, Zeming Lin, Natalia Gimelshein, Luca Antiga, et al. Pytorch: An imperative style, high-performance deep learning library. *Advances in neural information processing systems*, 32, 2019.

- [76] YOLOV5 github repository. <https://github.com/ultralytics/yolov5>, 2022.
- [77] Sankar K Pal, Anima Pramanik, Jhareswar Maiti, and Pabitra Mitra. Deep learning in multi-object detection and tracking: state of the art. *Applied Intelligence*, 51(9):6400–6429, 2021.
- [78] Anton Milan, Konrad Schindler, and Stefan Roth. Challenges of ground truth evaluation of multi-target tracking. In *Proceedings of the IEEE Conference on Computer Vision and Pattern Recognition Workshops*, pages 735–742, 2013.
- [79] Gioele Ciaparrone, Francisco Luque Sánchez, Siham Tabik, Luigi Troiano, Roberto Tagliaferri, and Francisco Herrera. Deep learning in video multi-object tracking: A survey. *Neurocomputing*, 381:61–88, 2020.
- [80] Harold W Kuhn. The hungarian method for the assignment problem. *Naval research logistics quarterly*, 2(1-2):83–97, 1955.
- [81] Pauli Virtanen, Ralf Gommers, Travis E. Oliphant, Matt Haberland, Tyler Reddy, David Cournapeau, Evgeni Burovski, Pearu Peterson, Warren Weckesser, Jonathan Bright, Stéfan J. van der Walt, Matthew Brett, Joshua Wilson, K. Jarrod Millman, Nikolay Mayorov, Andrew R. J. Nelson, Eric Jones, Robert Kern, Eric Larson, C J Carey, İlhan Polat, Yu Feng, Eric W. Moore, Jake VanderPlas, Denis Laxalde, Josef Perktold, Robert Cimrman, Ian Henriksen, E. A. Quintero, Charles R. Harris, Anne M. Archibald, Antônio H. Ribeiro, Fabian Pedregosa, Paul van Mulbregt, and SciPy 1.0 Contributors. SciPy 1.0: Fundamental Algorithms for Scientific Computing in Python. *Nature Methods*, 17:261–272, 2020.
- [82] Yunhao Du, Yang Song, Bo Yang, and Yanyun Zhao. Strongsort: Make deepsort great again. *arXiv preprint arXiv:2202.13514*, 2022.
- [83] A. Milan, L. Leal-Taixé, I. Reid, S. Roth, and K. Schindler. MOT16: A benchmark for multi-object tracking. *arXiv:1603.00831 [cs]*, March 2016. arXiv: 1603.00831.
- [84] P. Dendorfer, H. Rezatofighi, A. Milan, J. Shi, D. Cremers, I. Reid, S. Roth, K. Schindler, and L. Leal-Taixé. Mot20: A benchmark for multi object tracking in crowded scenes. *arXiv:2003.09003[cs]*, March 2020. arXiv: 2003.09003.
- [85] Alex Bewley, Zongyuan Ge, Lionel Ott, Fabio Ramos, and Ben Upcroft. Simple online and realtime tracking. In *2016 IEEE international conference on image processing (ICIP)*, pages 3464–3468. IEEE, 2016.
- [86] Mikel Broström. Real-time multi-camera multi-object tracker using yolov5 and strongsort with osnet. [https://github.com/mikel-brostrom/Yolov5\\_StrongSORT\\_OSNet](https://github.com/mikel-brostrom/Yolov5_StrongSORT_OSNet), 2022.
- [87] Steven L Brunton, Joshua L Proctor, and J Nathan Kutz. Discovering governing equations from data by sparse identification of nonlinear dynamical systems. *Proceedings of the national academy of sciences*, 113(15):3932–3937, 2016.
- [88] Anindya Chatterjee. An introduction to the proper orthogonal decomposition. *Current science*, pages 808–817, 2000.
- [89] J Nathan Kutz, Steven L Brunton, Bingni W Brunton, and Joshua L Proctor. *Dynamic mode decomposition: data-driven modeling of complex systems*. SIAM, 2016.

- [90] Peter J Schmid. Dynamic mode decomposition of numerical and experimental data. *Journal of fluid mechanics*, 656:5–28, 2010.
- [91] Erdi Kara. <https://github.com/erkara/trackingdroplets>, 2022.
- [92] Prasun Roy, Subhankar Ghosh, Saumik Bhattacharya, and Umapada Pal. Effects of degradations on deep neural network architectures. *arXiv preprint arXiv:1807.10108*, 2018.